UNIVERSITY OF SOUTHAMPTON

The cosmological evolution of the properties of powerful extragalactic radio sources and their environments

Yang Wang

Submitted for the degree of Master of Philosophy

SCHOOL OF PHYSICS AND ASTRONOMY

FACULTY OF SCIENCE

February 28, 2007

ABSTRACT

Radio galaxies and radio-loud quasars produce powerful collimated gas flows or jets interacting with the gas in their environments. Here we seek to develop a model for the evolution of the jet parameters and the properties of their environments during cosmological timescales. Combining the evolutionary model for individual radio sources from Kaiser, Dennett-Thorpe & Alexander (1997) with the Radio Luminosity Function from Willott et al. (2000), we perform multi-dimensional Monte Carlo simulations in order to compile artificial samples. We then compare their statistical properties with those of sources contained in the observed low frequency radio surveys, 3CRR, 6CE and 7CRS. We compare them on the radio luminosity (P) - linear size (D) diagram and use the two-dimensional Kolmogorov-Smirnov test to search for the best fitting parameters for each evolutionary model describing the source population as a whole. We find that the environments of radio sources evolve with cosmological time, in the sense that sources at high redshift are located in denser environments. However, we do not find a significant connection between the jet power and the density of the environment.

Contents

Preface

All work presented here has been carried out by the author, in collaboration with others, at University of Southampton between October 2005 and September 2006.

The observation samples the author used in this paper are provided by astronomy group of Oxford. Details of the data can be found online. The model for the evolution of FRII sources used here is presented by Kaiser & Alexander (1997) and Kaiser, Dennett-Thorpe & Alexander (1997). The author also uses Radio Luminosity Function presented by Willott et al. (2000). The Kolmogorov-Smirnov test mentioned in the paper is presented by Peacock (1983).

Acknowledgements

1   Introduction

The formation and evolution of massive galaxies are important components in understanding how the universe evolved. It is not clear why AGN formation take place at the centers of some galaxies, but it is believed that this occurs as part of all massive galaxies and jet activity is often associated with AGN. Some of the most distant and powerful active galaxies have been observed in the radio band and radio astronomy has been closely connected with cosmology since then.

Fanaroff & Riley (1974) split extragalactic radio sources into two classes depending on their large-scale morphology: FRI and FRII. FRI objects have bright cores and edge-darkened lobes while FRII objects have large-scale structures which are edge-brightened and contain hot spots. FRII are more luminous than FRI with a transition luminosity around $P_{178MHz} \sim 10^{25} WHz^{-1} sr^{-1}$. Owen & Ledlow (1994, hereafter OL94) found that the break in radio luminosity extends into the optical and FRIIs are associated with more optically-luminous galaxies. However, the break between FR classes increases with increasing optical luminosity of the host galaxies. The physics leading to the FRI-FRII transition is not well understood, but may depend on the gas density in the environment (e.g. Alexander 2000). In our work, we only concentrate on the FRII-type objects because we have good analytical models for them.

A large stellar mass implies a more massive galaxy which probably also implies a denser gas environment (O'Sullivan et al. 2001). More massive galaxies also contain more massive black holes at their centers (e.g. Kormendy & Richstone 1995). So we can expect that more powerful jets originate from black holes which are more massive and are located in denser environments. Together with the result from OL94, we expect that there is a connection between the jet properties and their environments. The aim of our work is to study if there is a connection or lack of a connection between jet properties, source environment and redshift of the sources.

In recent years, various samples of radio sources observed at low radio frequencies have been published like 3CRR, 6CE and 7CRS, which are all complete down to their flux-limits. These

samples indicate that the comoving density of radio galaxies was higher during the quasar era around redshift $z = 2$ as compared to the present epoch(e.g. Jackson & Wall 1999; Willott et al. 2001; Grimes, Rawlings & Willott 2004). The star and galaxy formation rate was also considerably higher in the quasar era. The radio luminosity function (RLF) has been developed as a tool to describe the densities of radio sources. Willott et al. (2000, hereafter W00) generated an RLF at $151 MHz$ which shows a peak at around $z = 2$. Optical and hard X-ray observations of powerful AGN also reveal a similar trend for the quasar era (e.g. Ueda et al. 2003).

Many analytical models for extragalactic classical double radio sources have been published which characterize radio sources in terms of their dynamics and radio luminosity evolution. In Figure 1, we show the structure of a typical FRII radio source. In this paper we use the model of Kaiser & Alexander (1997, hereafter KA97), which showed that the lobes inflated by the jets emerging from the AGN grow in a self-similar fashion. The radio lobe luminosity evolution is given by the following paper, Kaiser, Dennett-Thorpe & Alexander (1997, hereafter KDA97). The radio synchrotron emission of the lobes is due to relativistic electrons spiralling in the magnetic field of the lobe. This model self-consistently takes into account the energy losses of these electrons due to the adiabatic expansion of the lobes, synchrotron radiation and inverse Compton scattering of cosmic microwave background photons off the electrons.

The purpose of this work is to find the best fitting parameters describing the radio sources and their environments and how they evolve over cosmological time scales. My approach differs from that of Kaiser & Alexander (1999, hereafter KA99) who assume a 'birth function' to describe the probability of the radio sources progenitors becoming active and turning into radio sources. Their intrinsic luminosity evolution is determined by the properties of their jets and the environments the progenitors are located in at some cosmological epoch. We extend this work by directly using the RLF from W00 as a description of the birth function. Blundell & Rawlings (1999) try to explain the trend of radio galaxy properties with redshift. The main difference between their work and ours is that they use a model for the radio hot spots leading to steeper tracks in the P-D diagram. And they also do not consider the RLF directly like we do. Barai & Wiita (2005) test three existing evolutionary models for FRII sources and show none of them fit the observation, but they did not
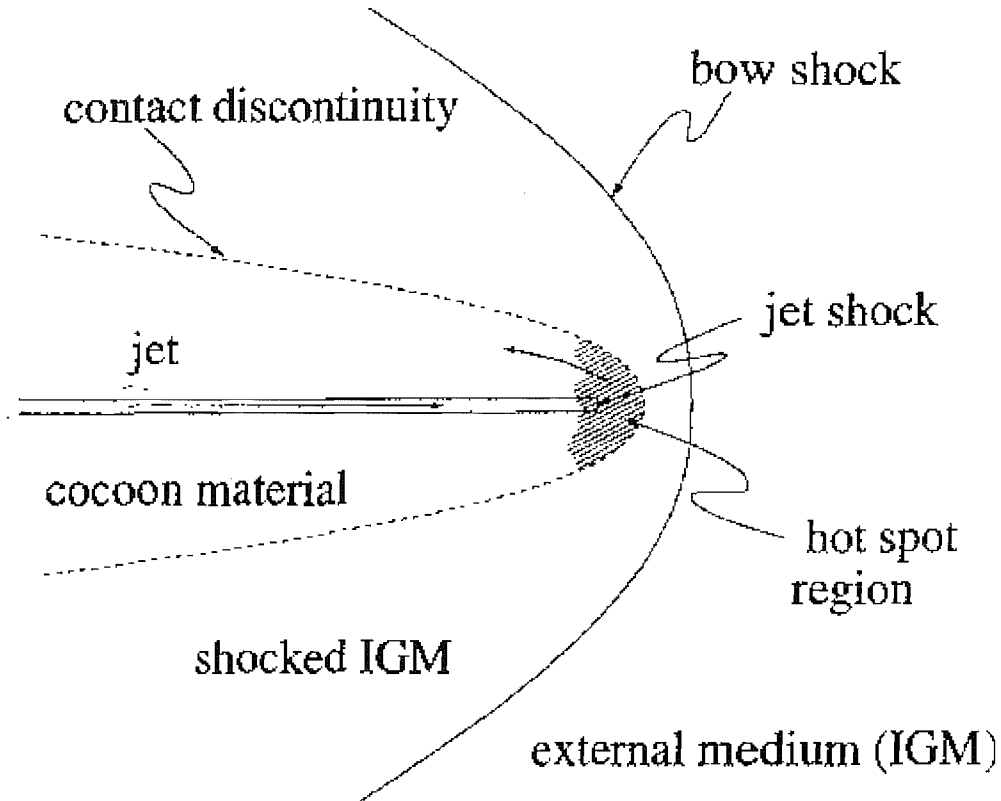
Figure 1: A cartoon of the jet and the intergalactic medium of an FRII source. A jet of constant Lorentz factor and power is decelerated in a hot spot converting energy into relativistic electrons and magnetic field. The jet is balanced by the pressure in the hot spot region, which expands self-similarly along with the bow shock and lobe. Synchrotron losses are important in the magnetic field, but adiabatic losses suffered in moving into the lobe. Once in the lobe, time-dependent synchrotron, inverse Compton and adiabatic losses determine the spatially integrated electron spectrum.

take into account of the RLF as well.

One of the most important tools to study the evolution of radio sources is the P-D diagram introduced by Shklovskii (1963). It is defined by plotting the radio luminosity at a specific frequency, P_ν, as a function of linear size of a source, D. Baldwin(1982) pointed out that it is analogous to the Hertzsprung-Russell diagram for stars. The source distribution in the P-D plane is a result of the intrinsic evolution of individual sources and the cosmological evolution of the source population as a whole. Since we may assume that source lifetimes are considerably shorter than the

age of the universe, the P-D diagram has been used to place some constraints on the evolution of individual sources (Baldwin 1982, Ueeser et al.) and to look for consistency between data and models (KDA97; Manolakou & Kirk 2002). We will use the P-D diagram populated by sources from observed, complete samples to constrain the parameters of our model.

In section 2 we will describe the KA97 and KDA97 model. Then we will introduce the RLF generated by W00 in section 3. Our prediction of the physical properties of radio sources and their cosmological evolution are discussed in section 4. In section 5 we will show the results of our Monte-Carlo simulation. Finally in section 6 we discuss the best fitting model parameters in the general context of AGN and their host galaxies. Throughout the paper we are using the cosmological model with $H_0 = 75 km s^{-1} Mpc^{-1}$, $\Omega_M = 0.3$, $\Omega_\Lambda = 0.7$.

2 Model for FRII sources

2.1 Dynamical model

The structure of FRII sources is formed by powerful jets which come from the supermassive black holes in the center of the radio galaxies. The jets end with a shock and form a hot spot which is very compact. Then the jet material inflates a lobe or cocoon around the jet, driving a bow shock into the surrounding gas. This basic idea was first proposed by Blandford & Rees (1974) and Scheuer (1974). Begelman & Cioffi (1989) give an analytical model of the cocoon of the radio sources. In their model the jet properties depend quite crucially on the geometry of the cocoon which is difficult to measure from observation. Falle (1991) developed a new model showing that the bow shock should be self-similar. KA97 extended this model assuming the pressure of the cocoon and the jet itself are equal and predicting that both the bow shock and the cocoon grow in a self-similar way if the surrounding gas decreases as $1/d^2$ or flatter. d is the radial distance from the AGN in the center of the source. Therefore we use the KA97 model in our work because it does not depend on the exact geometry of the cocoon and is easier to use. In the following I sketch the derivation of the model by KA97 and give a summary of those aspects of the model important for my own work.

KA97 simply use a power-law to describe the density of the atmosphere around the central AGN:

$$\rho_x = \rho_0 \left(\frac{d}{a_0}\right)^{-\beta},$$ (1)

where d is the radial distance from the core of the source, ρ_0 is a constant density, and a_0 is a scalelength. X-ray observations of the hot gas around galaxies imply that β should be distributed in the range $0 < \beta \leq 2$.

Assuming the rate of energy input into the cocoon is constant throughout the life time of the source and can be characterized by the jet power Q_0, then the length of the jet, L_j, can be written as:

$$L_j = c_1 a_0 \left(\frac{t}{\tau}\right)^{3/(5-\beta)},$$ (2)

where $\tau \equiv \left(\frac{a_0^5 \rho_0}{Q_0}\right)^{1/3}$ is a convenient time-scale, t is the age of the jet and c_1 is a constant.

The pressure of the cocoon, which is also the pressure of the jet, is constant throughout except the region near the hot spot. It can be written as:

$$p_c = \frac{18}{(\Gamma_x + 1)(5 - \beta)^2} \frac{c_1^{2-\beta}}{c_2} \theta^2 \rho_0 \left(\frac{a_0}{\tau}\right)^2 \left(\frac{t}{\tau}\right)^{(-4-\beta)/(5-\beta)} , \qquad (3)$$

where c_2 is a constant, θ is the opening angle of the jet and Γ_x is the adiabatic index of the gas surrounding the cocoon.

The constants c_1, c_2 and c_3 are given by:

$$c_1 = \left(\frac{c_2}{c_3 \theta^2} \frac{(\Gamma_x + 1)(\Gamma_c - 1)(5 - \beta)^3}{18(9(\Gamma_c + (\Gamma_c - 1)\frac{c_2}{4\theta^2}) - 4 - \beta)}\right)^{1/(5-\beta)} , \qquad (4)$$

$$c_2 = \left(\frac{(\Gamma_c - 1)(\Gamma_j - 1)}{4\Gamma_c} + 1\right)^{\Gamma_c/(\Gamma_c - 1)} \frac{\Gamma_j + 1}{\Gamma_j - 1}, \qquad (5)$$

$$c_3 = \frac{\pi}{4R_T^2} \approx \frac{\pi \theta^2}{c_2}, \qquad (6)$$

where Γ_c is the adiabatic index of the material in the cocoon and the approximation of equation (6) is valid for a roughly cylindrical cocoon.

The detailed calculation and discussion of the equations and constants above can be found in KA97.

2.2 The radio emission of the jet

Following this dynamical model, KDA97 extended the model to determine the radio emission of a radio source and track the luminosity evolution through the Power-Linear size (P-D) diagram.

At low frequencies, the total radio luminosity of the source is dominated by the emission of the cocoon in form of the synchrotron radiation. But the emission from the hot spot becomes

important at high frequencies. Here we only work at low frequencies as the model does not include the emission of the hot spots. Since we are considering the total source luminosity, we simply use the approximation that the electrons are emitting only at their critical frequency $\nu = \gamma^2 \nu_L$, where $\nu_L = \frac{eB}{2\pi m_e}$ is the Larmor frequency. So the total radio power at a given frequency is (e.g. Shu 1991):

$$P_\nu = \int \frac{c\sigma_T u_B}{6\pi} \frac{\gamma^3}{\nu} n(\gamma)\delta V, \tag{7}$$

where σ_T is the Thompson cross section, u_B is the energy density of the magnetic field, δV is a volume element of the cocoon, $n(\gamma)$ is the energy distribution of the relativistic electrons within δV, which is simply assumed to follow a power-law energy distribution at the initial time:

$$n(\gamma, t)d\gamma = n_0 \gamma^{-P} d\gamma. \tag{8}$$

γ is the Lorentz factor and evolves with time as the electrons lose their energy. The rate of change of the Lorentz factor is given by:

$$\frac{d\gamma}{dt} = -\frac{a_1}{3} \frac{\gamma}{t} - \frac{4}{3} \frac{\sigma_T}{m_e c} \gamma^2 (u_B + u_c). \tag{9}$$

The first term on the right hand side is due to the adiabatic expansion of the cocoon where the volume δV expands as $\delta V \propto t^{a_1}$. The second term due to the synchrotron radiation as well as the inverse Compton scattering of the CMBR. In the model, we assume the magnetic field to be completely tangled on scales much smaller than the size of the emission region. This allows us to treat the energy density of the magnetic field inside the emitting volume, u_B, as a function of age, t and adiabatic index, Γ_B, ($u_B \propto t^{-\Gamma_B a_1}$). The energy density of the CMBR, u_C, is a function of redshift ($u_C \propto (z + 1)^4$). Integration of equation (9) gives:

$$\frac{t^{-a_1/3}}{\gamma} - \frac{t_i^{-a_1/3}}{\gamma_i} = a_2(t, t_i), \tag{10}$$

where

$$a_2(t, t_i) = \frac{4\sigma_T}{3m_e c} \left(\frac{u_B(t_i)}{a_3} t_i^{a_1 \Gamma_B} (t^{a_3} - t_i^{a_3}) + \frac{u_C}{a_4} (t^{a_4} - t_i^{a_4}) \right), \tag{11}$$

with $a_3 = 1 - a_1(\Gamma_B + 1/3)$ and $a_4 = 1 - a_1/3$. The parameters here and in the following with indices i are for those at the initial time when the jet material is injected into the cocoon.

If $u_e(t_i)$ is the energy density of the relativistic electrons at time t_i, the normalization $n_0(t_i)$ in equation (8) can be written as:

$$n_0 = \frac{u_e(t_i)}{m_e c^2} \left(\int_{\gamma_{i,min}}^{\gamma_{i,max}} (\gamma_i - 1)\gamma_i^{-P} d\gamma_i \right)^{-1}, \tag{12}$$

where $\gamma_{i,min}$ and $\gamma_{i,max}$ are the lower and higher energy cut-off of the initial Lorentz factor distribution. The electrons are uniformly distributed over the volume δV. Because of the expansion of δV, we have to set $t^{a_1} n(\gamma, t) d\gamma = t_i^{a_1} n(\gamma_i, t_i) d\gamma_i$. So the energy distribution of the relativistic electrons at time $t > t_i$ is given by:

$$n(\gamma, t) d\gamma = n_0 \frac{\gamma_i^{2-p}}{\gamma^2} \left(\frac{t}{t_i} \right)^{-4a_1/3} d\gamma. \tag{13}$$

The contents of the cocoon can be divided into two separate 'fluids' with individual energy density: one consists of electrons and contributes an energy density u_e with adiabatic index Γ_e. The other is the magnetic field contributing an energy density u_B with adiabatic index Γ_B. The overall dynamics are governed by the pressure in the cocoon, $p_c = (\Gamma_c - 1)(u_B + u_e)$. With r being defined as the ratio of the energy density of the magnetic field to the energy density of the electrons, we have:

$$u_e(t_i) = \frac{p_c(t_i)}{(\Gamma_c - 1)(r + 1)}, \tag{14}$$

$$u_B(t_i) = \frac{r p_c(t_i)}{(\Gamma_c - 1)(r + 1)}. \tag{15}$$

Consider a volume element δV in the cocoon which is injected at time t_i during a short time interval δt_i. After t_i, δV expands adiabatically and so

$$\delta V(t) = \frac{(\Gamma_c - 1) Q_0}{p_c(t_i)} (4 R_T^2)^{\frac{1-\Gamma_c}{\Gamma_c}} \left(\frac{t}{t_i} \right)^{a_1} \delta t_i, \tag{16}$$

where $a_1 = (4 + \beta)/(\gamma_c(5 - \beta))$

Substitute equation (13) and equation (16) into equation (7), we get:

$$P_\nu = \int_{t_{min}}^{t} \frac{\sigma_T c r Q_0 n_0}{6 \pi \nu (r + 1)} (4 R_T^2)^{\frac{1-\Gamma_c}{\Gamma_c}} \frac{\gamma^{3-p} t_i^{\frac{a_1}{3}(p-2)}}{(t^{-\frac{a_1}{3}} - a_2(t, t_i) \gamma)^{2-p}} \left(\frac{t}{t_i} \right)^{-a_1(\frac{1}{3} + \Gamma_B)} dt_i \tag{17}$$

t_{min} is defined as the minimum injection time, t_i, of that part of the cocoon which is still radiating at observing frequency, ν. We set the observing frequency equal to the critical frequency of those electrons with the maximum Lorentz factor in this part of the cocoon.

2.3   Parameters used in our simulation

Before moving on to a description of our Monte Carlo simulation, we have to set the values of all the model constants and simplify the equations above.

We assume that the material in the jet and the cocoon as well as the magnetic field are all relativistic, giving the adiabatic indices $\Gamma_j = \Gamma_C = \Gamma_B = 4/3$, while the external medium is "cold", giving $\Gamma_x = 5/3$.

For external atmospheres with $\beta = 2$, take the adiabatic indexes above we get $c_1 = \left(\frac{64R_T^4}{3\pi(6+3R_T^2)}\right)^{1/3}$ from equation (4) and $c_2 = 7 \times \left(\frac{49}{48}\right)^4$ from equation (5). So the properties of the jet can be written as:

$$L_j = t_0 \left(\frac{64Q_0R_T^4}{3\pi(6 + 3R_T^2)}\right)^{1/3} (\rho_0 a_0^2)^{-1/3} \tag{18}$$

$$p_c = \frac{3}{16R_T^2}\rho_0 a_0^2 t_0^{-2} \tag{19}$$

Equation (17) is not analytically soluble for arbitrary p, but as the spectral indices of the observed radio sources infer $2 \le p \le 3$. For simplicity, We take $p = 2$, then we have the ratio of u_B and u_e, $r = \frac{u_B}{u_e} = (1 + p)/4 = 0.75$ according to the minimum energy argument. And equation (17) can be simplified to:

$$P_\nu = \int_{t_{min}}^t \frac{\sigma_T c Q_0 n_0 \gamma}{28\pi\nu}\left(\frac{t}{t_i}\right)^{-2.5} dt_i. \tag{20}$$

In our model, the initial power law of the energy distribution extends to $\gamma_{i,min} = 1$ and $\gamma_{i,max} = 10^5$ following the discussion in KDA97. Then n_0 given by equation (12) can now be written as:

$$n_0 = \frac{u_e(t_i)}{m_e c^2}(ln(\frac{\gamma_{i,max}}{\gamma_{i,min}}) + \gamma_{i,max}^{-1} - \gamma_{i,min}^{-1})^{-1} \approx \frac{u_e(t_i)}{m_e c^2}(5ln10 - 1)^{-1}. \tag{21}$$

γ in equation (20) can be calculated from the assumption that all electrons only radiate at their critical frequency:

$$\gamma = \sqrt{\frac{\nu}{\nu_L}} = \sqrt{\frac{2\pi m_e \nu}{eB}} = \sqrt{\frac{2\pi m_e \nu}{e \sqrt{2\mu_0}}}u_B(t)^{-0.5} \tag{22}$$

For $u_B \propto t^{-\Gamma_B a_1}$, the Lorentz factor of the relativistic electrons that were accelerated at the time t_i which are now, at time t, radiating at the observing frequency v, is given by:

$$\gamma = \sqrt{\frac{2\pi m_e v}{e\sqrt{2\mu_0}}} u_B(t_i)^{-0.25} t_i^{-0.5} t^{0.5},$$ (23)

where t is the life time of the radio source. Together with equation (20) and equation (21), we finally get:

$$P_v = \frac{2\sqrt{2}\sigma_T Q_0 A^{0.75}}{63ct^2(5ln10 - 1)\sqrt{m_e\pi ev}\sqrt{2\mu_0}}(t^{1.5} - t_{min}^{1.5})$$ (24)

where A is given as a function of the pressure of the cocoon, p_c, and the life time of the jet, t:

$$A = \frac{27\theta^2 \rho_0 a_0^2}{28c_2} = \frac{9p_c}{7}t^2.$$ (25)

2.4 Calculation of t_{min}

As the jet radiates, the Lorentz factor of the electrons becomes smaller and smaller. The population injected into the cocoon before a minimum injection time, t_{min}, will no longer contribute to the luminosity at a certain frequency. This happens when the critical frequency of the electrons with the maximum Lorentz factor, γ_{max}, falls below the observing frequency, v. So we have to consider t_{min} as the lower limit of the integration in equation (20)

For the definition of A in last section, the equations (10) and (11) give:

$$\gamma_{max} = \frac{\gamma_{i,max} t^{-0.5}}{\gamma_{i,max} a_2(t, t_{min}) + t_{min}^{-0.5}} = \frac{\gamma_{i,max} t^{-0.5}}{-B(t^{-1.5} - t_{min}^{-1.5}) + C(t^{0.5} - t_{min}^{0.5}) + t_{min}^{-0.5}},$$ (26)

where B and C are defined as: $B = \frac{8\sigma_T \gamma_i A}{9m_e c}$, $C = \frac{8\sigma_T u_c \gamma_i}{3m_e c}$

Now we can build up a connection between the emission frequency, v and the minimum injection time t_{min}, if we know the life time of the jet:

$$v = \gamma_{max}^2 v_L = \frac{e\sqrt{2\mu_0 A}\gamma_{i,max}^2 t^{-2}}{2\pi m_e(-B(t^{-1.5} - t_{i,min}^{-1.5}) + C(t^{0.5} - t_{i,min}^{0.5}) + t_{i,min}^{-0.5})^2}$$ (27)

We present an analytic solution for t_{min} of this equation in appendix 1.

There are four free parameters through out the calculation above. So if we set the redshift, z, the pressure of the cocoon, p_c and the life time of the jet, t_0, we can get all the properties of a radio source at the observing frequency, which is $151MHz$ in our simulation work.

3   Radio luminosity function at 151MHz

The radio luminosity function (RLF) is defined as the number of radio sources per unit co-moving volume per unit logarithm(base 10) of luminosity, $\rho(L, z)$. The shape and evolution of the RLF provide important constraints on the nature of radio activity in massive galaxies and its cosmic evolution. The first comprehensive study of the RLF was performed by Dunlop & Peacock (1990), hereafter DP90. They used several complete samples selected at $2.7GHz$ with flux limits ranging from $2.0Jy$ to $0.1Jy$, and considered the flat- and steep-spectrum population separately, then derived the RLF for each population. The result of DP90 indicated that the co-moving number density have a 'redshift cut-off' at z 2. An upgrade work of DP90 can be found in Dunlop (1998), and a critical re-evaluation of the evidence for a redshift cut-off in the flat-spectrum population can be found in Jarvis & Rawlings (2000). Because the KA97 model only calculates the emission of the cocoon which dominates at low frequency, the samples such as those produced by the Cambridge group over the past decades, which were compiled at $151MHz$ and $178MHz$ are most appropriate for our work. Willott et. al. (2000), hereafter W00, use these samples and derive the RLF of steep-spectrum radio sources at low frequency.

3.1   Complete samples

Complete sample means the sample consists of every radio source in a well-defined area in the sky above a specified flux limit at the observing frequency. All the sources are identified optically with a galaxy or quasar and the redshifts together with the linear sizes of the large-scale radio structure are determined. The three complete samples used in W00 are from the 7CRS, 6CE and 3CRR surveys. The luminosity-redshift plane for the three samples is shown in Figure 2.

7CRS: The Seventh Cambridge Redshift Survey is a combination of the sub-divisions I,II and III of the original 7C survey (McGilchrist et al. 1990). It contains every source with a flux-density $S_{151} \geq 0.5Jy$ in three regions of the sky covering a total of $0.022sr$. However, the linear size, D, and the spectral index at $151MHz, \alpha_{151}$, for 7c-I and II have not been published yet. So we only use 7C-III in our comparison of observed sample with simulated samples. The relevant sample
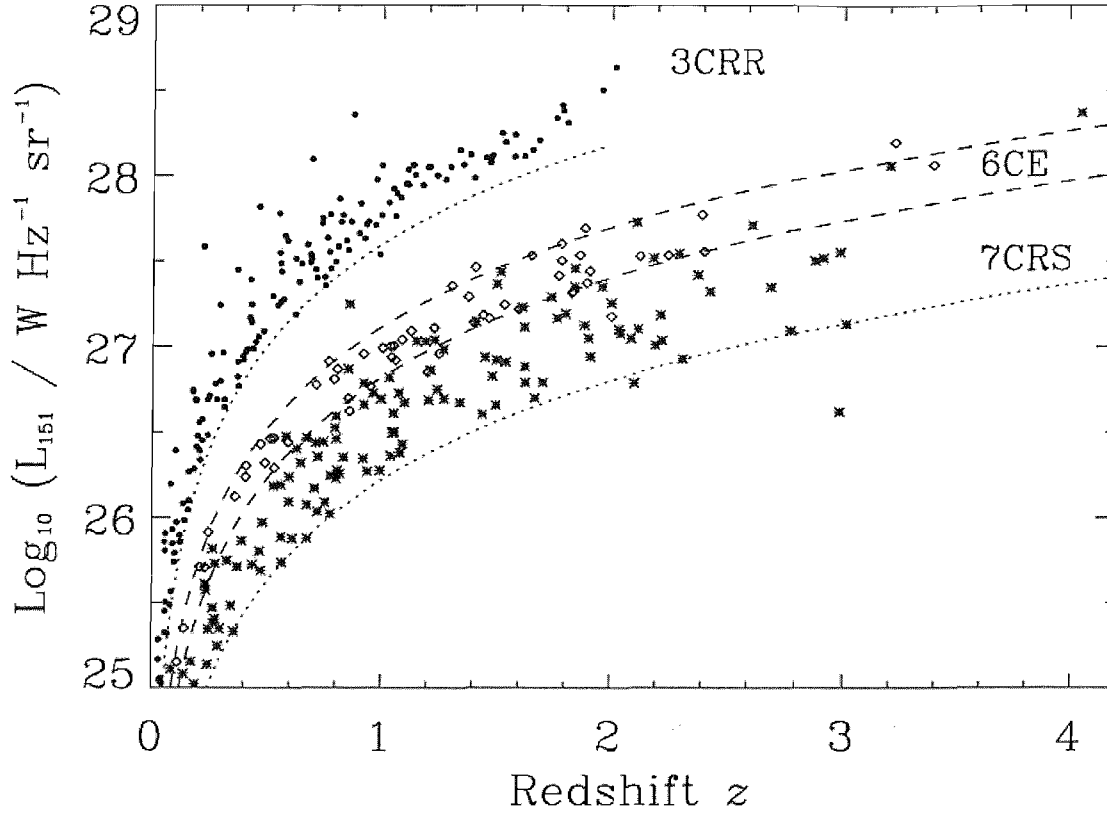
Figure 2: The radio luminosity-redshift plane for the 3CRR, 6CE and 7CRS samples. The different symbols identify sources from different samples: 3CRR (filled circles), 6CE (open diamonds) and 7CRS (asterisks). The dotted lines show the lower limits on the flux-density for the 3CRR and 7CRS samples and the dashed lines the limits for the 6CE sample. (This plot is for $\Omega_M = 1$, $\Omega_\Lambda = 0$.) This diagram is from W00

can be found in Table 9 of Lacy et al. (1999).

6CE: The Sixth Cambridge radio survey by Eales(1985) is the original 6C survey. It was reselected and updated by Rawlings, Eales & Lacy (2001). The flux-limits of this sample are $2.0 \leq S_{151} \leq 3.93 Jy$ and the sky area covered is $0.103 sr$.

3CRR: The Third Cambridge Revised Revised sample covers the largest sky area ($4.23 sr$) of the three samples, but is not as deep as the other two. It is observed at a frequency of 178MHz with a flux limit $S_{178} > 10.9 Jy$. W00 simply assume a typical spectral index of 0.8 to transfer the radio luminosity from $178 MHz$ to $151 Mhz$.

Table 1: Observational Samples			
Survey	Flux Limit (Jy)	N0. of Sources	Sky Area (sr)
3CRR	$S_{178} > 10.9$	145	4.23
6CE	$2 \leq S_{151} \leq 3.93$	58	0.102
7CRS	$S_{151} > 0.5$	128	0.022
7CI	$S_{151} \geq 0.51$	37	0.0061
7CII	$S_{151} \geq 0.48$	40	0.0069
7CIII	$S_{151} > 0.5$	51	0.009

The information for these three samples are listed in Table 1. Because the KA97 model does not include the low luminosity FRI sources, we only discuss FRII sources in this paper, and only listed the number of FRII sources in Table 1.

3.2   The shape of the RLF

With a totally 356 sources from the three samples, W00 model the RLF with two distinct populations of radio sources which allowed to have different shapes and evolutionary properties.

The low-luminosity radio source population is composed of FRIs and low-excitation/weak emission line FRIIs. It can be modeled by a Schechter function:

$$\rho_l(L) = \rho_{l0} \left(\frac{L}{L_{1\star}} \right)^{-\alpha_1} exp \left(\frac{-L}{L_{1\star}} \right) \tag{28}$$

where $\rho_l(L)$ is the source number density as a function of radio luminosity L, ρ_{l0} is a normalization term, $L_{1\star}$ is the break luminosity and α_1 is the power-law slope. The evolution function of ρ_l is modeled as $f_1(z) = (1 + z)^{k_1}$ up to a maximum redshift, z_{l0}, beyond which there is no further evolution. Hence there are five free parameters to be fixed for the low-luminosity population.

For the high-luminosity population, a similar form is adopted:

$$\rho_h(L) = \rho_{h0} \left(\frac{L}{L_{h\star}}\right)^{-\alpha_h} exp\left(\frac{-L_{h\star}}{L}\right),$$ (29)

where the index h refers to the high luminosity population. It is expected that $L_{l\star} \approx L_{h\star}$, so that there is no discontinuity or bimodality in the RLF as suggested by observations.

The high-luminosity population is assumed to undergo density evolution, so we require a term for redshift evolution, $f_h(z)$, here. We just describe the model C in W00, which is used in my simulation work. The model gives the z-distribution having a one-tailed Gaussian rise to the peak redshift and then a one-tailed Gaussian decline at higher redshifts which is allowed to have a different width from the rise. It directly fits the strength of any decline in the co-moving density beyond the peak redshift z_{h0}, since the value of the high-redshift Gaussian width z_{h2} is free to be fit from 0 for an abrupt cut-off to a large value for a very gradual decline at high redshift. Hence there are a total of six free parameters in the high-luminosity population model.

Below we summarize and list all the equations for the RLF. The total space density of all radio sources is:

$$\rho(L, z) = \rho_l + \rho_h,$$ (30)

where

$$\rho_l = \rho_{l0} \left(\frac{L}{L_{l\star}}\right)^{-\alpha} exp\left(\frac{-L}{L_{l\star}}\right)(1 + z)^{k_1}, \qquad for \qquad z < z_{l0},$$ (31)

$$\rho_l = \rho_{l0} \left(\frac{L}{L_{l\star}}\right)^{-\alpha} exp\left(\frac{-L}{L_{l\star}}\right)(1 + z)^{k_{l0}}, \qquad for \qquad z \geq z_{l0},$$ (32)

$$\rho_h(L) = \rho_{h0} \left(\frac{L}{L_{h\star}}\right)^{-\alpha_h} exp\left(\frac{-L_{h\star}}{L}\right) f_h(z).$$ (33)

The functions, $f_h(z)$, can have different forms for the different models considered by W00. For model C:

$$f_h(z) = exp(-\frac{1}{2}(\frac{z - z_{h0}}{z_{h1}})^2), \qquad for \qquad z < z_{h0},$$ (34)

$$f_h(z) = exp(-\frac{1}{2}(\frac{z - z_{h0}}{z_{h2}})^2), \qquad for \qquad z \geq z_{h0}.$$ (35)

For a cosmological model with $H_0 = 50 kms^{-1}Mpc^{-1}$, $\Omega_M = 1$, $\Omega_\Lambda = 0$ and $\Omega_k = 0$, W00 gives the best-fit parameters: $log(\rho_{l0}) = -7.120$, $\alpha_1 = 0.539$, $log(L_{l\star}) = 26.10$, $z_{l0} = 0.706$, $k_l = 4.30$,

$log(\rho_{h0}) = -6.196$, $\alpha_h = 2.27$, $log(L_{h\star}) = 26.95$, $z_{h0} = 1.91$, $z_{h1} = 0.559$, $z_{h2} = 1.378$. The shape of the RLF is shown in Figure 3.
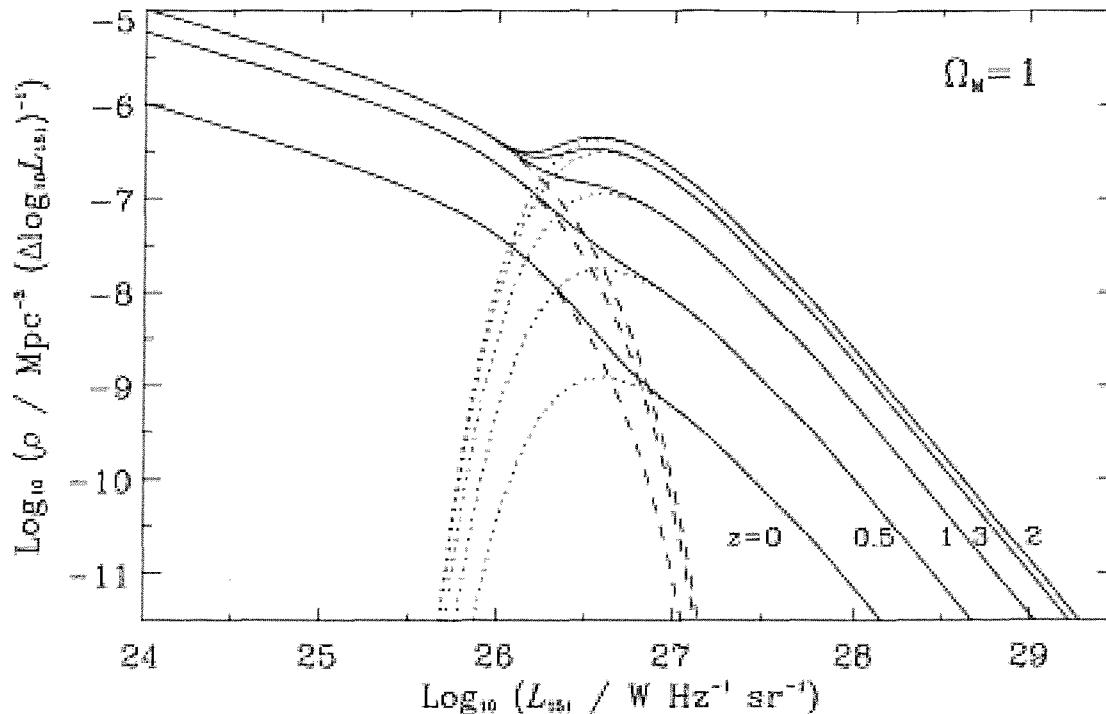
Figure 3: The radio luminosity function derived for model C for $\Omega_M = 1$. Dashed lines show the low-luminosity population. The dotted lines refer to the high-luminosity population. Solid lines show the sum of both components. Figure reproduced from W00

Because the individual model we are using in this work can only be applied to FRII sources, we will not use the whole RLF and only concentrate on the FRII sources. Here we simply assume that the portion of FRI sources is twice as much as that of the FRII sources in the low-luminosity population, which consists of both kind of sources. So we use the RLF for FRII sources as $\rho = \rho_l/3 + \rho_h$. This portion is just an assumption and can be changed for better fit in the future work if necessary.

3.3 Transfer of the RLF to a different cosmological model

Because in this paper we use the cosmological model with $\Omega_M = 0.3$, $\Omega_\Lambda = 0.7$ and $\Omega_k = 0$, $H_0 = 75 km s^{-1} Mpc^{-1}$, we should transfer the RLF following the relation from Peacock (1985):

$$\rho_1(L_1, z)\frac{dV_1}{dz} = \rho_2(L_2, z)\frac{dV_2}{dz}, \tag{36}$$

where L is the luminosity derived from the flux density and redshift, and V is the comoving volume. The index 1 refers to the cosmological model used by W00 and 2 refers to the cosmological model used in this work.

Hogg (1999) defines different distances between two points in a given cosmology. The comoving distance, D_M, and the luminosity distance, D_L, with $\Omega_k = 0$ are given by:

$$D_M(z) = \frac{c}{H_0} \int_0^z \frac{dz'}{\sqrt{\Omega_M(1 + z')^3 + \Omega_\Lambda}}, \tag{37}$$

$$D_L(z) = \frac{c(1 + z)}{H_0} \int_0^z \frac{dz'}{\sqrt{\Omega_M(1 + z')^3 + \Omega_\Lambda}}, \tag{38}$$

where z is the redshift, c is the speed of light, and H_0 is the Hubble constant. Since the flux density, $S = LD_L^{-2}$, is a fixed parameter which comes from observation, the relation between L_1 and L_2 of a radio source at redshift z can be written as:

$$L_1 D_{L1}^{-2} = L_2 D_{L2}^{-2}. \tag{39}$$

Substituting equation (38) into equation (39) we get:

$$\frac{L_1}{L_2} = 2.25(\int_0^z \frac{dz'}{\sqrt{0.3(1 + z') + 0.7}})^{-2}(\int_0^z \frac{dz'}{\sqrt{(1 + z')^3}})^2 \tag{40}$$

The comoving volume element, dV, is given by:

$$dV = 4\pi D_M^2 dD_M. \tag{41}$$

Substituting equation (37) into equation (41), we get:

$$\frac{dV_1}{dV_2} = 2.25(\frac{\int_0^z \frac{dz'}{\sqrt{(1+z')^3}}}{\int_0^z \frac{dz'}{\sqrt{0.3(1+z')+0.7}}})^2 \sqrt{\frac{0.3(1 + z)^3 + 0.7}{(1 + z)^3}}. \tag{42}$$

Using equation (37) and equation (40), we can now easily transfer the RLF between the different cosmological models.

4 Evolutionary models

Now that we have a model for the evolution of individual FRII sources and the function describing their population, we proceed to generate large radio source populations by Monte-Carlo simulation.

4.1 Parameter setting

The main input parameters characterizing a source are the source age, t_0, redshift, z, radio luminosity, P, and the pressure of the cocoon, p_c. Each simulated source is assumed to evolve according to the KA97 model discussed in section 2. The range over which the input parameters used in the model vary can be constrained from observations. However, the constraints obtained in this way are incomplete and we will later find that there may also be considerable variation with redshift. The model describes the source evolution at a frequency measured in the rest frame of the source. So if the frequency of observation is $151MHz$, and a source is observed at redshift z, then the observed emission is emitted at a frequency $\nu_{rest} = 151 \times (1 + z)MHz$.

Since the observed RLF, $\rho_{z,P}$, gives the number density of sources with a certain redshift and luminosity, we first choose z and P in convenient steps. We then calculate the number in the relative volume element predicted by the RLF, $n = \rho_{z,P}dPdV$, so that the relative number of sources with different z and P in our artificial sample will fit the observations. We choose the cosmological age from $z = 4$ to $z = 0$, and the radio luminosity at $151MHz$ from $10^{24}W$ to $10^{29}W$ with a step of $10^{24}W$. This range covers all the sources in the three observed samples. In order to avoid very large sizes of the artificial samples, we normalize n and generate a random number between 0 and 1. If the random number is less than the renomalized n, then the source with that z and P will be included in our sample.

For the aspect ratio of the cocoon, R_T, we use a uniform distribution with $1.3 \leq R_T \leq 6.0$, taken from Leahy & Williams (1984). Next, we consider the distribution of t_0 and p_c. Alexander & Leahy (1987) give the upper limit of observed spectral ages $t_{0,max} = 10^9yr$, and more recent

investigations involving X-ray activity in AGN (Barger et al. 2001), SDSS optical studies of active galaxies (Miller et al. 2003) and black hole demographics arguments (e.g., Marconi et al. 2004) all support values in excess of $10^8 yr$. So we assume $t_{0,max}$ is between $10^8 yr$ and $10^9 yr$, but we test which value provides the best fit to the observations (see below). For sources reaching the maximum age we assume that the jet ceases to supply the cocoon with energy. The subsequent drop in radio luminosity occurs fast, because of the adiabatic expansion of the cocoon. We therefore assume that the radio luminosity of a source of age $t_{0,max}$ drops to zero instantaneously. For each source included in the artificial sample we choose a uniformly distributed random value in range $0 \leq t_0 \leq t_{0,max}$, we can estimate a reasonable value for the maximum pressure allowed in the cocoon from minimum energy considerations. This gives the minimum magnetic field strength as:

$$B_{min} = 1.8 \left(\frac{\eta L_\nu}{V} \right)^{2/7} \nu^{1/7} T. \tag{43}$$

So the pressure from the magnetic field which dominates the pressure of the cocoon is:

$$p_{mag} = \frac{B_{min}^2}{2\mu_0} = \frac{3.24 * \left(\frac{L_\nu}{c_3} \right)^{4/7} \nu^{2/7}}{2\mu_0 L_j^{12/7}}, \tag{44}$$

where ν is the observing frequency which is $151 MHz$ here, L_ν is the radio luminosity at that frequency which is between $10^{24} W Hz^{-1} sr^{-1}$ and $10^{29} W Hz^{-1} sr^{-1}$, L_j is the linear size of the jet which is between $1 kpc$ and $10^4 kpc$. From the equation and values above, we can get a range of $1 \times 10^{-16} \leq p_c \leq 1 \times 10^{-8} kgm^{-1} s^{-2}$. The details of the minimum energy argument can be found in Volume 2 of High Energy Astrophysics (Longair 1994). Because the early universe is much different from the local one, these two parameters should evolve with redshift, and we will consider different models with different forms of evolution. The details of the models will be discussed later in section 4.2. In general, we assign a uniformly distributed, random value of p_c from within the allowed range defined by the current model to each artificial source.

With the values of the parameters randomly generated above, we can calculate the linear size, L_j, and the jet power, Q_0, for each source to be included in the artificial sample from the KA97 model. Not all values are acceptable. Considering the break between the FRI and FRII sources, there should be a lower limit of the jet power for FRII sources. For the upper limit of jet power, we consider the Eddington luminosity limit, which gives the maximum luminosity at which a object with a given mass can radiate. In our work, we set $Q_{0,min} = 10^{37} W$ and $Q_{0,max} = 5 \times 10^{40} W$. If

the calculated Q_0 is not in this range, we regenerate the random parameters for the source with the same z and P until an acceptable combination of parameters is found.

Each model gives the total linear size of a radio source, but sources are randomly oriented in the sky, with an angle to the line of sight. The viewing angle, α_v, is distributed according to $sin\alpha_v d\alpha_v$ over the range 0 to $\pi/2$ radians. So the observed length of the jet is, $L_o = L_j \times sin(\alpha_v) = L_j \times \sqrt{r_N(2 - r_N)}$, where r_N is an uniform random number between 0 and 1. For simplicity, hereafter we denote the L_o as just L_j.

We will use Monte-Carlo simulation to generate our artificial samples. The whole process is shown in the flow diagram below.

$\longrightarrow$ choose P_z, z from min to max value, with certain step

$\downarrow$

calculate flux, s

$\downarrow$

$\xleftarrow{\text{no}}$ if s is above the flux limit

yes $\downarrow$

use RLF to calculate ρ

$\downarrow$

ρ multiply comoving volume to get a number, n

$\downarrow$

generate a random number, r_N

$\downarrow$

$\xleftarrow{\text{no}}$ if r_N is smaller than n

yes $\downarrow$

generate random t_0, p_c $\longleftarrow$

$\downarrow$ $\uparrow$

calculate t_{min}, Q_0

$\downarrow$ $\uparrow$

test if Q_0 is in the range $\xrightarrow{\text{no}}$

yes $\downarrow$

$\longleftarrow$ calculate L_J and plot the source on the P-D diagram
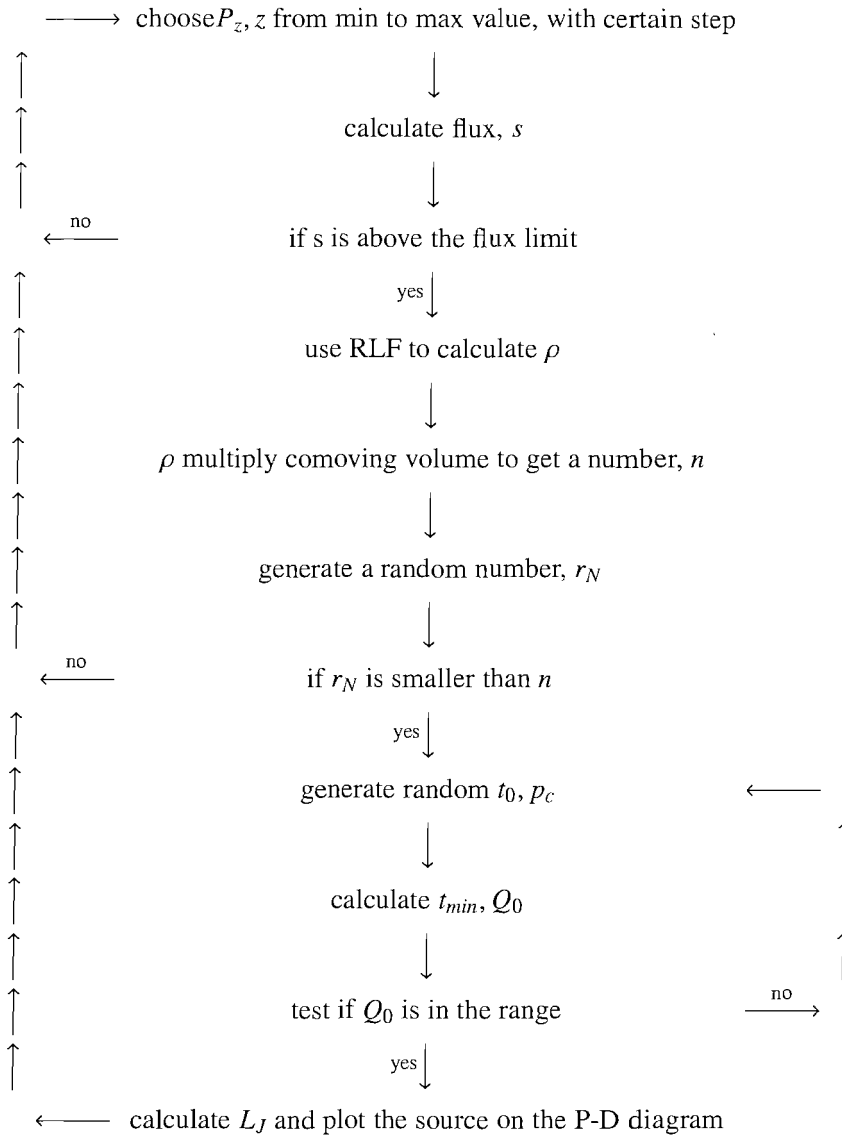
4.2 Evolutionary models

Before explaining the models we investigate in detail, we summarize the input parameters discussed in section 4.1:

We iterate redshift, z, and radio luminosity, P, from lower limit to upper limit step by step.

The aspect ratio of the cocoon, R_T, and the viewing angle, α_v, are taken from uniform distributions in a fixed range.

The life time of the jet, t_0, and the pressure of the cocoon, p_c are taken from uniform distribution between 0 and a maximum value. The maximum value can have different forms according to different models.

We now proceed to describe these models. In all models r_N denotes a uniformly distributed random number in the range 0 to 1

Model A: The simplest way we can assume is that there is no cosmological evolution. t_0 and p_c are uniformly distributed between 0 and a certain maximum value,

$$t_0 = r_N t_{0,max}, \tag{45}$$

and

$$p_c = r_N p_{c,max}. \tag{46}$$

Model B: Because the environment density of the early universe is likely to be higher than the local one, we assume the maximum value of p_c to increase with the redshift and evolved as a power-law of $1 + z$. For the aspect of the age of the jet, as the Jet power, Q_0, gives the rate of energy input the cocoon, so the source with more powerful jets may have shorter life time. We also know from KDA97 that Q_0 is the most important factor in determining the radio luminosity

of a given source. So for model B we assume that the maximum value of t_0 is influenced by P.

$$t_0 = r_N t_{0,max}(P/P_0)^{\alpha}, \tag{47}$$

and

$$p_c = r_N p_{c,max}(1 + z)^{\beta}. \tag{48}$$

Model C: The equation $p_c = 3\rho_0 a_0^2 t_0^{-2}/16R_T$ from the KA97 model shows that p_c is also affected by t_0 and R_T. So we introduce a new parameter $\Lambda = 3\rho_0 a_0^2/16$, where ρ_0 is a constant density, and a_0 is a scalelength. Because we have already assumed the evolution of t_0 and the uniform distribution of R_T, we vary model B by assuming that only the maximum value of Λ evolves with redshift. Therefore we take the distributions given in equations (49) and (50) for model C:

$$t_0 = r_N t_{0,max}(P/P_0)^{\alpha}, \tag{49}$$

$$p_c = r_N \Lambda_{max}(1 + z)^{\beta}(R_T t_0)^{-2}. \tag{50}$$

4.3   Kolmogorov-Smirnov test

After we generate the artificial sample we plot the sources on the P-D diagram and check the distribution to see how it compares to the observed samples. We need a technique to test how well they fit each other. For this we use a two-dimensional version of the Kolmogorov-Smirnov test.

The classical one-dimensional Kolmogorov-Smirnov test makes use of the probability distribution of the quantity D_{KS}, defined as the largest absolute difference between the cumulative frequency distributions of the parent population and that of an n-point simulated sample. Since D_{KS} turns out to be approximately proportional to $1/\sqrt{n}$, one usually refers to the probability distribution of the quantity $Z_n \equiv D_{KS}\sqrt{n}$. For large n ($n \geq 80$), the integral probability distribution $P(> Z_n)$ has the asymptotic expression(see Kendall & Stuart 1979),

$$P(> Z_n) = 2\sum_{k=1}^{\infty}(-1)^{k-1}exp(-2k^2 Z_n). \tag{51}$$

Peacock(1983) extend this to a two-dimensional test by making use of the maximum absolute difference D_{BKS} between the observed and simulated distributions, when all four possible ways to cumulate data following the directions of the coordinate axes are considered. In practice, Peacock's test requires that the cumulative distributions should be calculated in all $4n^2$ quadrants of the plane defined by,

$$(x < X_i, y < Y_j), (x < X_i, y > Y_j), (x > X_i, y < Y_j), (x > X_i, y > Y_j), \qquad (52)$$

for all possible combinations of the indexes i and j from 1 to n. Fasano & Franceschini (1987) develop a new version of this technique and make use of the total number of points in each of the four quadrants around a given point (x_i, y_i). They sum up observed data and model predictions only in the four quadrants of the plane defined by,

$$(x < X_i, y < Y_i), (x < X_i, y > Y_i), (x > X_i, y < Y_i), (x > X_i, y > Y_i), \qquad (53)$$

where i runs from 1 to n. They then calculate the largest absolute difference of the quantities from the real and artificial samples (both normalized to 1) within all four quadrants and define D_{BKS} as the largest of these differences when all data points are considered. Like in the one-dimensional case, we define $Z_n \equiv D_{BKS} \sqrt{n}$, where for a two-sample two-dimensional KS test $n \equiv n_1 n_2/(n_1 + n_2)$, where n_1 and n_2 are the number of the data points in each sample.

For our work the coordinate axes are given by the linear size and the radio luminosity. In practice, we apply the two-dimensional Kolmogorov-Smirnov test as follows:

(1) Find D_{BKS}, the maximum absolute difference in the two cumulative probability distributions being compared, where we consider all four possible ranking combinations.

(2) Set $Z_n = \sqrt{n}D_{BKS}$ and convert Z_n to Z_∞ by $1 - Z_n/Z_\infty = 0.53n^{-0.9}$, where for a two-sample test, $n = n_1 n_2/(n_1 + n_2)$

(3) Calculate the significance from $P(> Z_\infty) = 2exp[-2(Z_\infty - 0.5)^2]$. This probability will be too large by at very most a factor of ~ 1.5 and generally within ~ 1.1.

The full details of the process and the result above can be found in Peacock (1983).

5   Monte-Carlo simulation and test result

First we describe the density and probability contour plots we use to show the simulation result.

Because the Monte-carlo simulations give thousands of sources in one artificial sample, showing the data in the number density contour way is much clearer than plotting individual sources. We divide the P-D diagram into small bins and count the number of sources in each bin, then draw the density contours. Different contours imply different number density, the values from outside to inside are in the order of 1%, 10%, 40%, 80% of the maximum value. We then plot the sources from the observed samples on the same diagram for comparison.

Similarly, as there are too many free parameters we can set, we use probability contours to show the KS test results. The values of probability that the contours show from outside to inside are in the order of 1%, 10%, 20%.

5.1   Model A

This is a model with no cosmological evolution. There are only two free parameters to restrict the artificial sample: The maximum value of the lifetime of the jet, $t_{0,max}$ and the maximum value of the pressure of the cocoon, p_c. The KS test shows that the probabilities for these model are almost 0 for all $t_{0,max}$ from $10^8 yr$ to $10^9 yr$ and $p_{c,max}$ from $10^{-16} kgm^{-1} s^{-2}$ to $10^{-8} kgm^{-1} s^{-2}$. We show the number density contour of one of these artificial samples in Figure 4. In the diagram, we plot the radio luminosity of the samples directly at their observing frequency which is $178 MHz$ for 3CRR and $151 MHz$ for 6CE. In this way, we reduce a step of transferring luminosity between different frequencies and the result should be better. We will do this as well for model B and model C. From Figure 4, we can see the artificial sample do not fit the observation samples at all. The almost linear trend of luminosity with linear size is caused by the flux limit sources at high redshift must be more luminous to be included in the sample. They therefore require larger jet powers which lead to larger linear sizes on average.

Figure 4: The upper pane shows the P-D diagram of the 3CRR sample while the bottom one is the 6CE sample with source density contours from model A. The parameters we use here are $t_{0,max} = 5 \times 10^8 yr$ and $p_{c,max} = 1 \times 10^{-12} kgm^{-1}s^{-2}$. Crosses indicate FRII sources in the observed samples. Gray scales indicate the number density, the values from outside to inside are in the order of 1%, 10%, 40%, 80% of the maximum value

5.2 Model B

Once we begin to consider the evolution of the parameters throughout cosmological time, the simulation results become much better. Figure 5 shows the number density contours for the best fitting model. KS test shows the probability is around 0.5% and the parameter values are $\alpha = 0.1$, $\beta = 6.0$, $t_{0,max} = 5 \times 10^8 yr$, $p_{c,max} = 1 \times 10^{-13} kgm^{-1}s^{-2}$. The main problem with this model is that the population of the artificial sources with high luminosity, mainly located at large redshift, shows too small a distribution in linear size.

5.3 Model C

When we assume that only Λ, which gives some idea of the density of the jet environment, evolves with redshift, the distribution of the high luminosity population is wider (see Figure 6). In this model $t_{0,max}$ depend strongly on α and the best fitting value is at $\alpha = 0.2$. In Figure 7 we show the results and correlation of the model parameters for different β, $t_{0,max}$ and Λ_{max} with fixed α. We generate samples β from 2.0 to 5.8 with a step of 0.2, $t_{0,max}$ from $2 \times 10^8 yr$ to $5 \times 10^8 yr$ with a step of $1 \times 10^8 yr$ and three Λ_{max} values: $1 \times 10^{18}, 5 \times 10^{18}, 1 \times 10^{19} kgm^{-1}$. It is interesting to note that $t_{0,max}$ and β are correlated. Large values of β imply that the density in the environment of source at large redshift is larger than that at lower redshift. Consequently, sources at large redshift take longer to grow and hence require more time to reach a given length. As radio luminosity is lightly connected to redshift in our samples, it is not surprising to find the correlation of $t_{0,max}$ and β.

We do not show the simulation results for the 7CRS sample in this section, because the KS test shows that for all the models, the probability is not as good as the other two samples. The reason may be that the area covered by 7CRS is too small. We will discuss this point further in the next section.
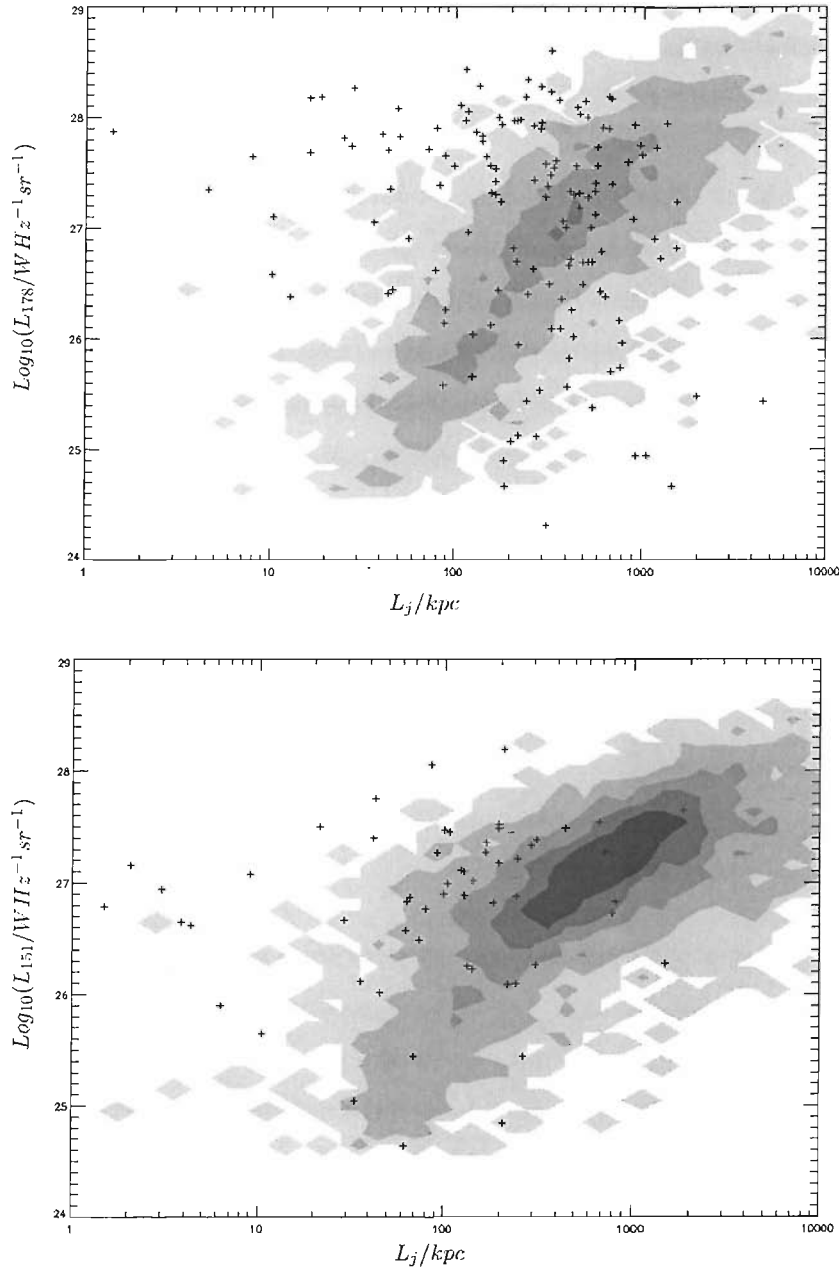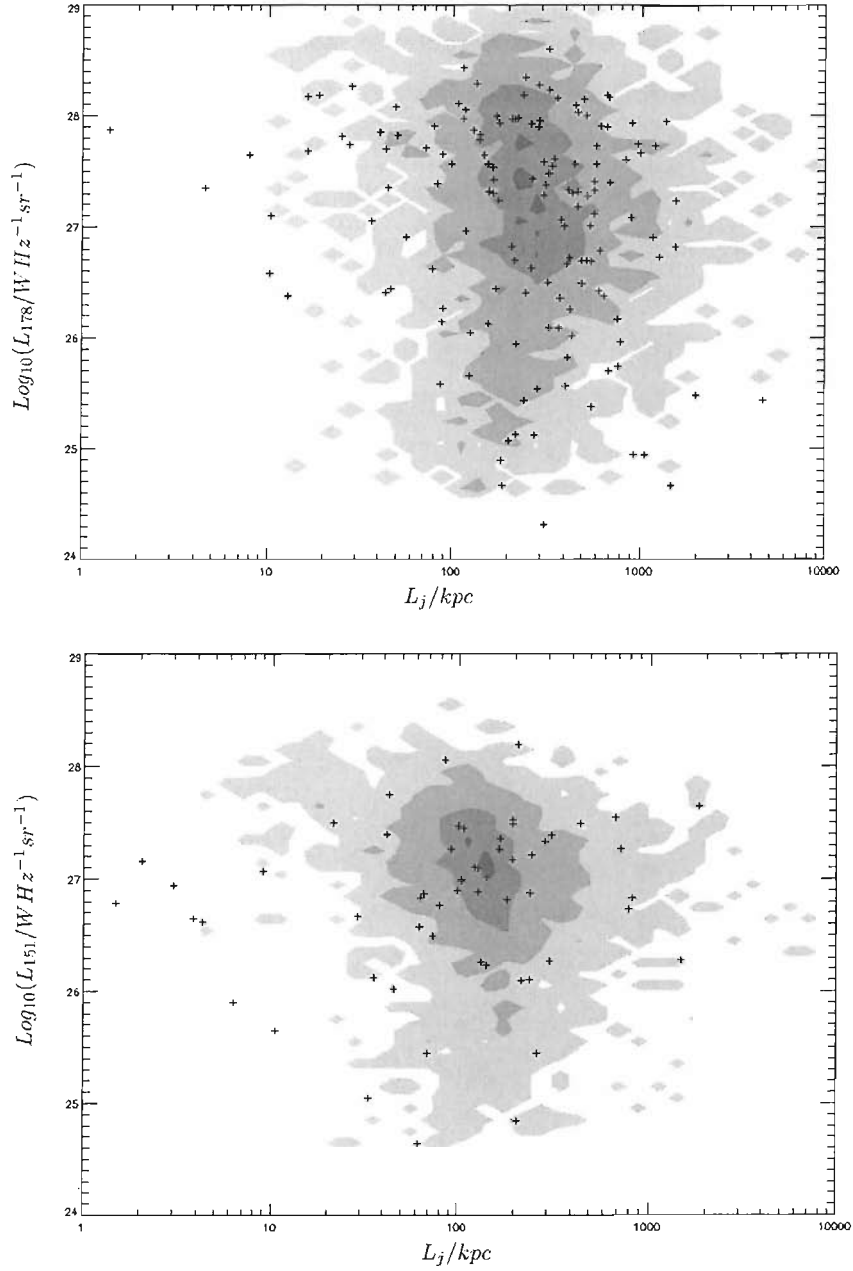
Figure 5: The upper pane show the P-D diagram of the 3CRR sample while the bottom one is the 6CE sample with source density contours from model B. The parameters we use here are $\alpha = 0.1, \beta = 6.0, t_{0,max} = 5 \times 10^{8} yr, p_{c,max} = 1 \times 10^{-13} kgm^{-1} s^{-2}$.Crosses indicate FRII sources in the observed samples. Gray scales indicate the number density, the values from outside to inside are in the order of 1%, 10%, 40%, 80% of the maximum value
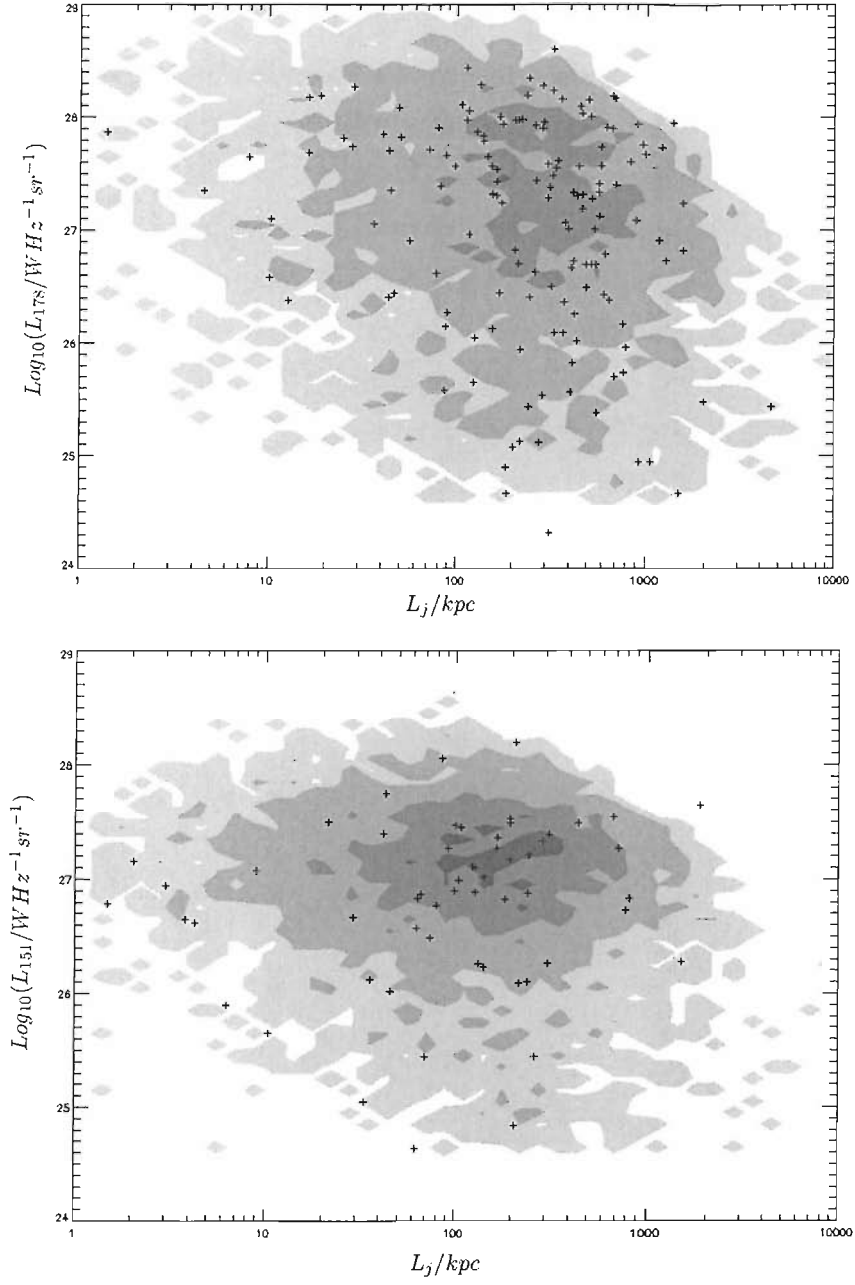
Figure 6: The upper pane shows the P-D diagram of the 3CRR sample with $\alpha = 0.2, \beta = 2.2,$ $t_{0,max} = 3 \times 10^8 yr, \Lambda_{max} = 5 \times 10^{18} kgm^{-1}$ while the bottom one is the 6CE sample with $\alpha = 0.2,$ $\beta = 2.2, t_{0,max} = 2 \times 10^8 yr, \Lambda_{max} = 5 \times 18^{18} kgm^{-1} s^{-2}$. Both artificial samples here are based on model C. Crosses indicate FRII sources in the observed samples. Gray scales indicate the number density, the values from outside to inside are in the order of 1%, 10%, 40%, 80% of the maximum value
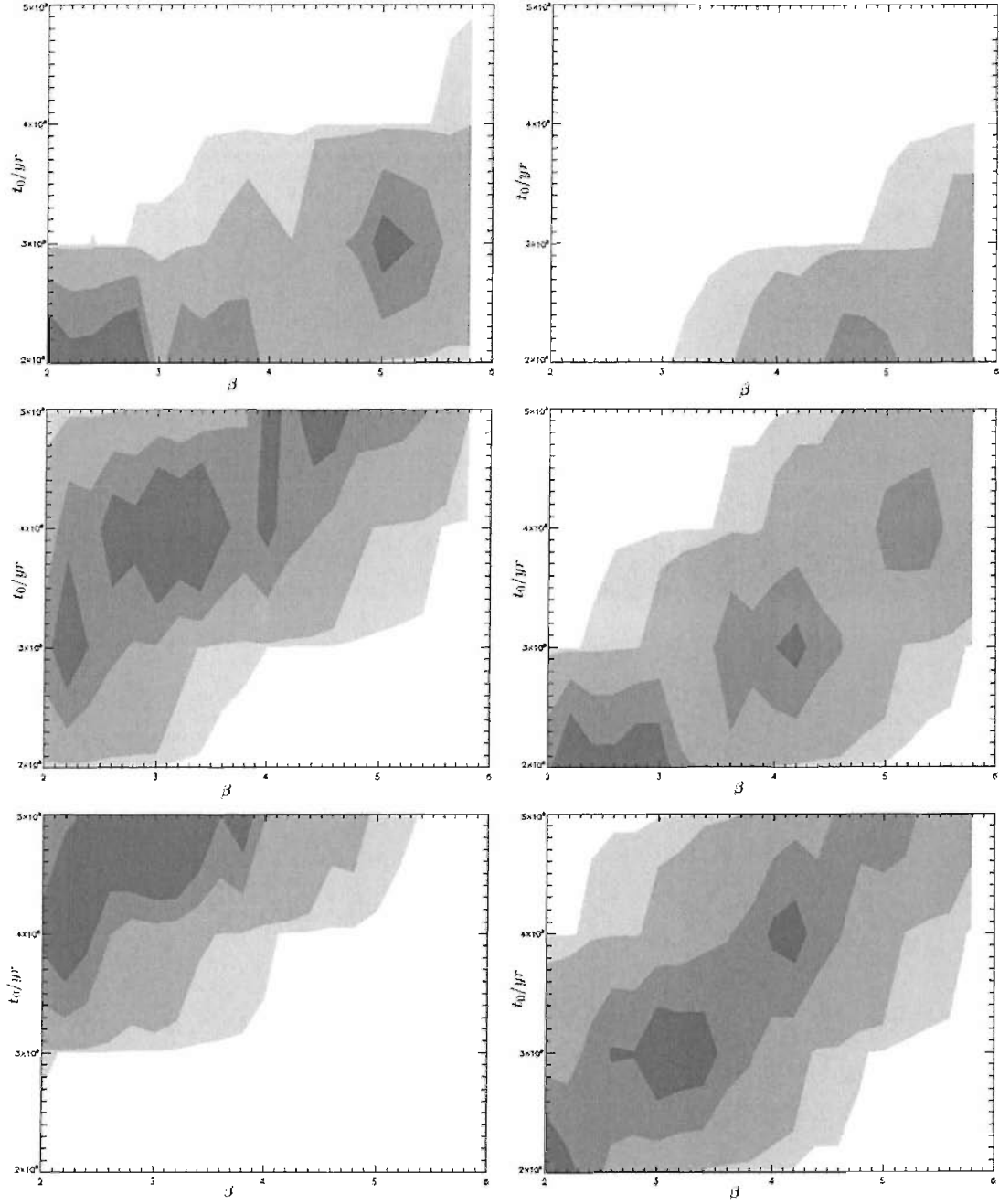
Figure 7: Probability contours for model C. The left three panes are for the 3CRR sample while the right three are for the 6CE sample. The panes from top to bottom are with different Λ_{max}. The values are $\Lambda_{max} = 1 \times 10^{18}, 5 \times 10^{18}, 1 \times 10^{19} kg m^{-1}$. The gray scales are probability contours. The values they show from outside to inside are in the order of 1%, 10%, 20%. There is a 'patchy' appearance on the diagram, it is mainly because the step of $t_{0,max}$ we chose is too big, we will test a smaller step in our future work.

6 Conclusion and discussion

During our multi-dimensional Monte-Carlo simulations, we find that the best fitting model and parameters show that the environment and the life time of the radio sources undergo a evolution throughout the cosmological timescales. For 3CRR and 6CE samples, we can get very good fits: The KS test gives a probability of 58% for $\alpha = 0.2$, $\beta = 3.2$, $t_{0,max} = 5 \times 10^8 yr$, $\Lambda_{max} = 1 \times 10^{19} kgm^{-1}$ for 3CRR and 37% for $\alpha = 0.2$, $\beta = 2.2$, $t_{0,max} = 2 \times 10^8 yr$, $\Lambda_{max} = 5 \times 10^{18} kgm^{-1}$ for 6CE. We now consider another sample roughly equivalent to 3C for comparison. This is the BRL sample, defined by Best, Rottgering and Lehnert(1999, hereafter BRL99) with 178 objects and a flux limit of $S_{408} \geq 5Jy$. We compare the BLR sample with the 3CRR sample in the P-D plane in the same way that we use to compare our artificial samples with 3CRR. The KS test shows the agreement between 3CRR and BRL is 46%. This shows that our best fitting artificial sample agrees with the observations to a degree similar to the agreement between similar observed samples drawn from the same source population. Figure 8 show the sources of 3CRR and BRL on the P-D diagram.

We notice that in different models, the best fitting values for different samples are different. The probability contours for all show that the best fitting values for the model parameters follow a linear distribution and are almost parallel to each other for 3CRR and 6CE. But they are not very far away from each other if we apply model C. Both the probabilities reaches up to 30% with $\alpha = 0.2$, $\beta = 2.2$, $t_{0,max} = 2.5 \pm 0.5 \times 10^8 yr$ and $\Lambda_{max} = 5 \times 10^{18} kgm^{-1}$, although the probability depends strongly on $t_{0,max}$. The probability contours show a trend that the model fits may be improved by allowing β and $t_{0,max}$ to decrease below the currently used minimum values. We will test this in the future even if most t_0 will fall below $10^8 yr$ and so may lie below the minimum ages of radio sources indicated by observations.

We can not get a good fit for the 7CRS sample from any of the models. The maximum probability is around 0.5%. The main reason for this should be the area covered by 7CRS is only $0.009 sr$ which is much smaller than that of 3CRR ($4.23 sr$) and 6CE ($0.109 sr$). The RLF may give the number of sources with a certain radio luminosity in the small reign covered by the sample as
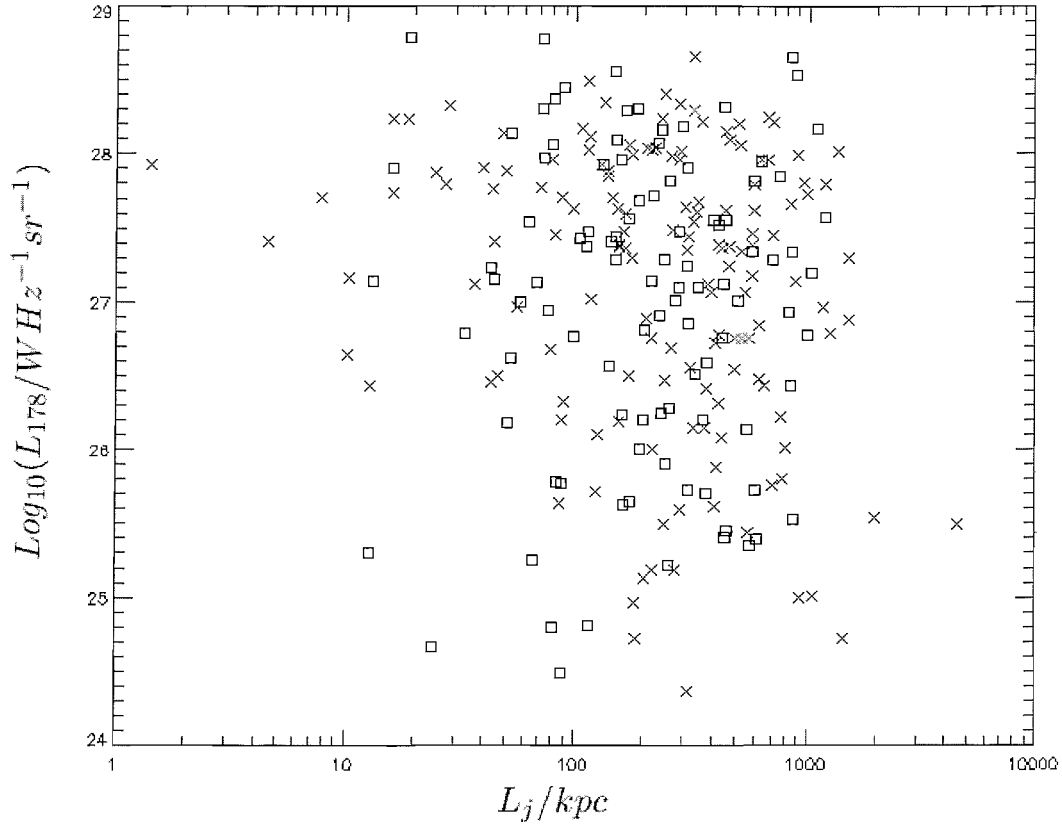
Figure 8: 3CRR and BRL objects in the P-D diagram at 178MHz. Cross symbols refer to 3CRR while squares refer to BRL. We convert the BRL sources from $408MHz$ to $178MHz$ by using their individual spectral indexes given by BRL99.

less than unity and so the sources in 7CRS are less representative of the entire population. Here, we show the 7CRS sample and one of the best fitting artificial 7CRS samples in Figure 9. We can see there happens to be a gap around $L_{151} = 10^{27} WHz^{-1} sr^{-1}$ and $L_j = 100kpc$ where we expect the highest source density according to 3CRR and 6CE samples.

The model shows that the life times of the jets evolve with redshift. Radio sources in the early universe have shorter life times. However, as the jets at high redshift are more luminous and considering the description function of model C, this trend is better to be explained by the more luminous sources having shorter lift times. The more powerful the jets of a source are, the shorter the jet activity can last.
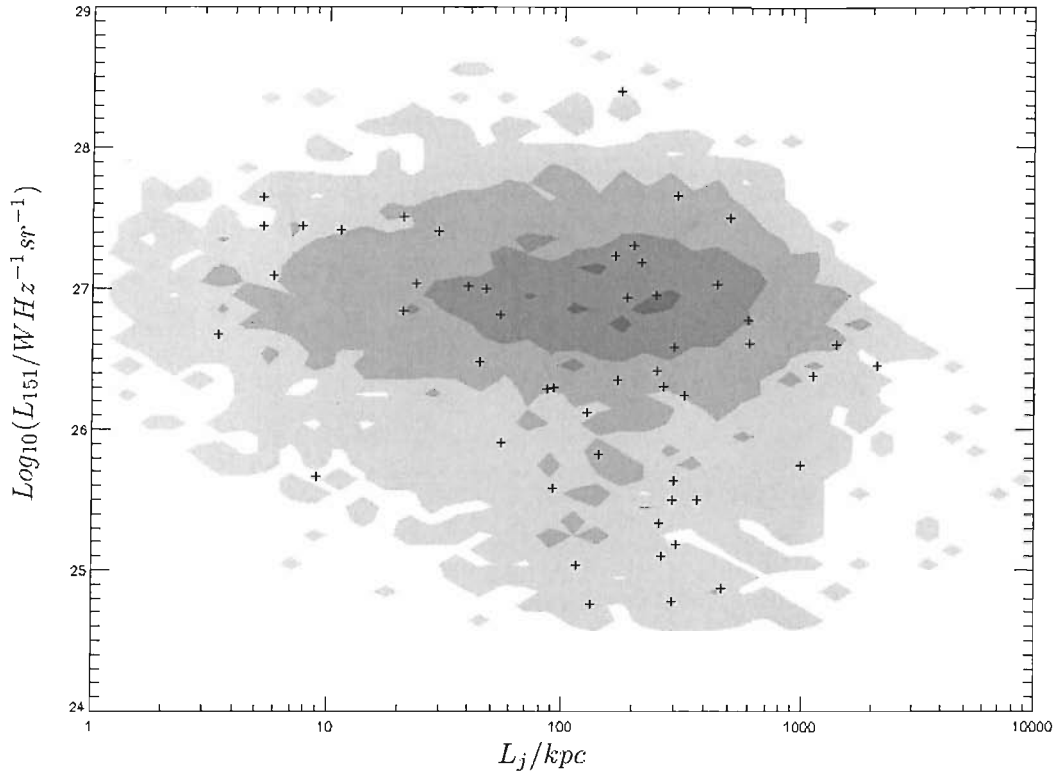
Figure 9: Density contour for 7CRS. This artificial sample comes from model C with $\alpha =$ $0.2, \beta = 2.2, t_{0,max} = 2 \times 10^8 yr, \Lambda_{max} = 5 \times 10^{18} kg m^{-1}$

The source environments also show strong evolution with cosmological time. Now we will discuss how they are connected with the jet power. First we show the relation between the jet power and the radio luminosity in Figure 10. We can see there is a significant connection. The sources with higher power have higher radio luminosity. It's not surprised to get this relation because the KDA97 model we are using have predicted it in their equation (16).

Figure 11 shows the relation between the jet power, radio luminosity and $\Lambda = 3\rho_0 a_0^2/16$. Because a_0 is a scale length and equal to $2kpc$ for most elliptical galaxies, we can say that Λ just implies the density of the jet environment. We notice that there is a limit line at the lower right corner of the diagram. It arises from the function that describes the evolutionary model together with the flux limit of the sample. The model requires big Λ located in early universe and only the sources with a luminosity above the flux limit can be observed. We show the power-Λ diagram of 6CE sample in Figure 12. We can find that when the flux limit is lower, the limit line in the dia-
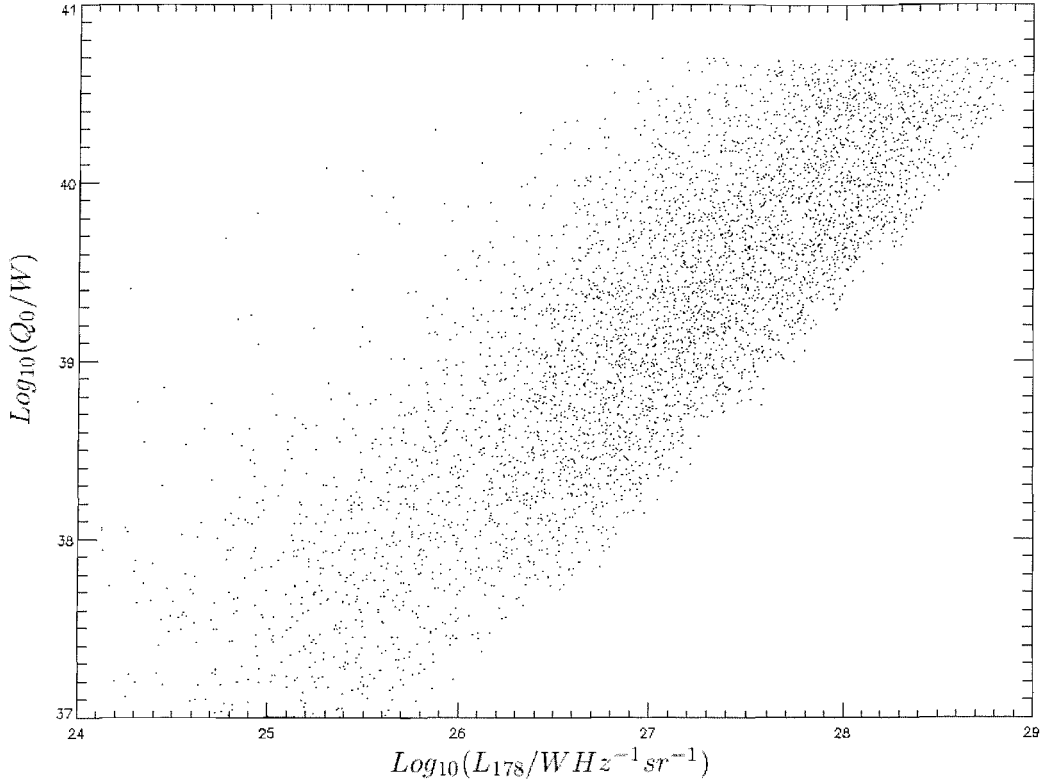
Figure 10: Radio luminosity(P)-jet power(Q_0) diagram. The sample we use is the artificial 3CRR sample with $\alpha = 0.2, \beta = 2.2, t_{0,max} = 3 \times 10^8 yr, \Lambda_{max} = 5 \times 10^{18} kgm^{-1}$. The KS test gives the probability of this sample compared to the observed 3CRR sample is 31%. All of the analysis in this section related to 3CRR is based on this artificial sample
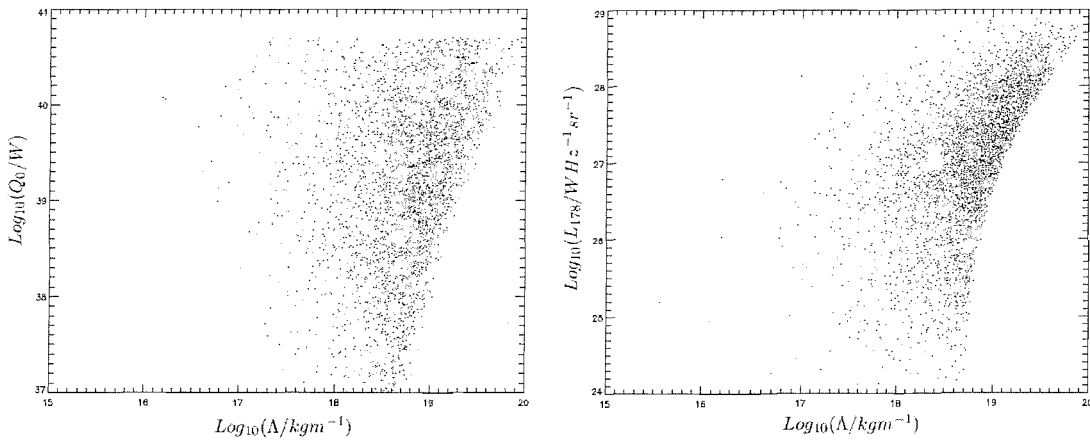
Figure 11: The left pane compares the jet power Q_0 with the density parameter Λ and the right one shows the radio luminosity P against Λ
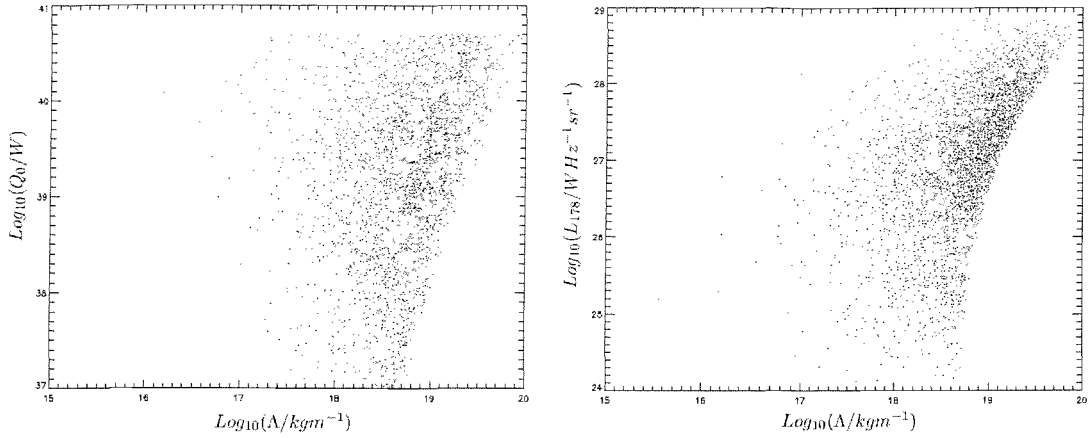
Figure 12: The Q_0-Λ and P-Λ diagram for 6CE sample with $\alpha = 0.2$, $\beta = 2.2$, $t_{0,max} = 2 \times 10^8 yr$, $\Lambda_{max} = 5 \times 10^{18} kgm^{-1}$.
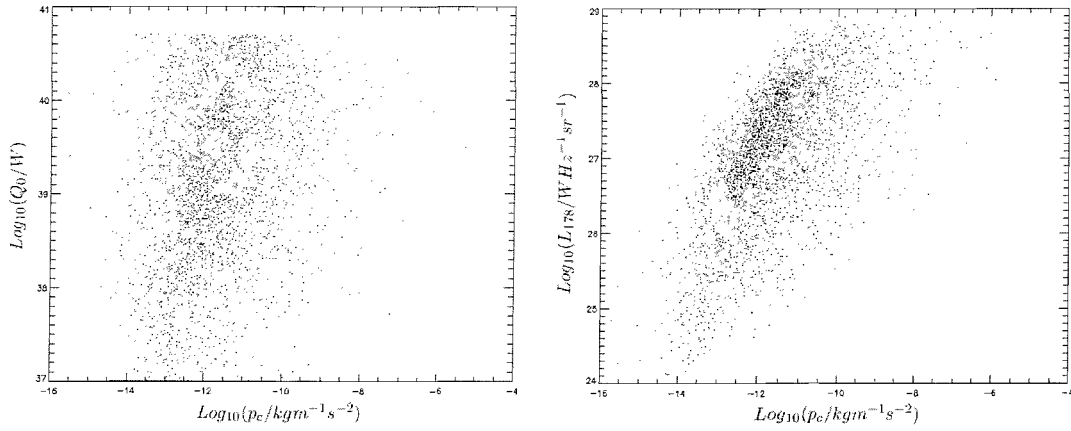
Figure 13: The left pane shows the relation between Q_0 and p_c and the right one shows that between P and p_c

gram goes lower. So we can not say there is a significant connection between the jet power and the density of the jet environment. This does not agree with the result from Allen et al. (2006) which shows that the jet power is close related to the Bondi accretion rate decided by the environment density. But in their paper, all the sources they use is FRI while in our paper we use FRII. KA99 also show this connection but where is a similar limit line in their work and they did not take into account of the selection effect properly.

Figure 13 is like Figure 11, but Λ is replaced by the pressure of cocoon, p_c. We find a strong

correlation. Comparison of Figure 11 and Figure 13 shows that the jet power and the radio luminosity are more directly connected with the lobe pressure as expected from the model of KDA97. As we have to take into account the age of the jet when transferring between lobe pressure and environment density, the relation with Λ is not so significant.

Now we have developed the cosmological evolution model of the radio galaxy environment which fits the observed samples well. We will try different evolutionary models for t_0 and p_c in the future, for example, t_0 is influenced not by the radio luminosity but by the redshift. There are many other jet evolution models different from KA97, like Blundell, Rawlings & Willott (1999) and Manolakou & Kirk (2002). We will extend this work by doing similar test on these models. We will also take account of the first and second fields of the 7C survey so that it may give a better representation of the total population and get better fit. Once we know the environment evolution well, we can discuss the formation and evolution of the AGNs in the center of radio galaxies which are closely connected with the material around them. Our final goal is to consider the role that the radio galaxies play in the cosmological history of the universe.

Appendix 1: Calculate t_{min} at 151MHz

Take $v = 151MHz$ in the equation (27), we will get the equation of the minimum injection time:

$$E t_{min}^{0.5} = B t_{min}^{-1} - C t_{min} + 1, \qquad (1)$$

where

$$D = \sqrt{\frac{e \sqrt{2\mu_0 A \gamma_{i,max}^2} t^{-2}}{2\pi m_e v}}, \qquad (2)$$

and

$$E = D + B t^{-1.5} - C t^{0.5}. \qquad (3)$$

Setting $x = \sqrt{t_{min}}$ and rearranging, we get a fourth-order equation:

$$C x^4 + E x^3 - x^2 - B = 0. \qquad (4)$$

Now set

$$y = x + \frac{E}{4C} \qquad (5)$$

and substitute back into equation(57), we get:

$$y^4 + P y^2 + Q y + R = 0, \qquad (6)$$

with

$$P = -\frac{1}{c}\left(\frac{3E^2}{8C} + 1\right), \qquad (7)$$

$$Q = \frac{E}{c^2}\left(\frac{E^2}{8C} + \frac{1}{2}\right), \qquad (8)$$

$$R = -3\frac{E^4}{256C^4} - \frac{E^2}{16C^3} - \frac{B}{C}. \qquad (9)$$

There should be four solutions of this equation given by:

$$y_1 = \frac{1}{2}\left(\sqrt{-P+\alpha} + \sqrt{-P-\alpha + \sqrt{\alpha^2 - 4R}}\right), \qquad (10)$$

$$y_2 = \frac{1}{2}\left(-\sqrt{-P+\alpha} + \sqrt{-P-\alpha + \sqrt{\alpha^2 - 4R}}\right), \qquad (11)$$

$$y_3 = \frac{1}{2}\left(\sqrt{-P+\alpha} - \sqrt{-P-\alpha + \sqrt{\alpha^2 - 4R}}\right), \qquad (12)$$

$$y_4 = \frac{1}{2}\left(-\sqrt{-P+\alpha} - \sqrt{-P-\alpha + \sqrt{\alpha^2 - 4R}}\right), \qquad (13)$$

where α is the solution of a so-called cubic resolvent given by:

$$\alpha^3 - P\alpha^2 - 4R\alpha + 4PR - Q^2 = 0. \qquad (14)$$

I

What we need is a real solution among the y_i which should lie between 0 and the life time of the jet. So next we need to find the real solution of the cubic equation.

Setting $\beta = \alpha - \frac{1}{3}P$ and the cubic equation can be written as:

$$\beta^3 + M\beta + N = 0, \tag{15}$$

with

$$M = -\frac{P^2}{3} - 4R, \tag{16}$$

$$N = \frac{8}{3}PR - Q^2 - \frac{2}{27}P^3. \tag{17}$$

The determinate of this reduced cubic equation is given by:

$$\Delta = \left(\frac{M}{3}\right)^3 + \left(\frac{N}{2}\right)^2. \tag{18}$$

If $\Delta \geq 0$, then the real solution is given by:

$$\beta = \left(-\frac{N}{2} + \sqrt{\Delta}\right)^{1/3} + \left(-\frac{N}{2} - \sqrt{\Delta}\right)^{1/3}. \tag{19}$$

If $\Delta < 0$, where will be no real solution.

Appendix 2: 3CRR sample

Name	z	S_{178}/Jy	α_{151}	$\theta/arcsec$
4C12.03	0.156	10.90	0.870	240.00
3C6.1	0.840	14.93	0.554	26.00
3C9	2.012	19.40	0.813	14.00
3C13	1.351	13.08	0.753	28.10
3C14	1.469	11.33	0.760	24.00
3C16	0.406	12.20	0.954	78.00
3C19	0.482	13.18	0.637	6.80
3C20	0.174	46.76	0.606	53.10
3C22	0.937	13.18	0.785	24.40
3C28	0.195	17.76	1.011	43.40
3C33	0.059	59.29	0.701	257.00
3C33.1	0.181	14.17	0.834	238.70
3C34	0.689	12.97	1.029	46.70
3C35	0.067	11.44	0.907	730.00
3C41	0.794	11.55	0.721	25.00
3C42	0.395	13.08	0.705	31.00
3C43	1.47	12.64	0.756	2.50
3C46	0.437	11.11	0.905	164.00
3C47	0.425	28.77	0.994	77.70
3C49	0.621	11.22	0.410	1.01
3C55	0.735	23.43	0.725	71.00
3C61.1	0.188	34.00	0.736	186.00
3C65	1.176	16.56	0.498	17.40
3C67	0.3102	10.90	0.809	2.30
3C68.1	1.238	13.95	0.736	52.00
3C68.2	1.575	10.90	0.962	22.30
3C79	0.255	33.24	0.794	88.70
3C98	0.031	51.44	0.732	307.50
3C109	0.305	23.54	0.806	96.00
4C14.11	0.207	12.09	0.840	115.00
3C123	0.218	206.01	0.652	41.10
3C132	0.214	14.93	0.790	22.30
3C138	0.759	24.19	0.225	0.65
3C147	0.545	65.94	0.137	3.00
3C153	0.277	16.67	0.577	9.26
3C171	0.238	21.25	0.731	10.00

Name	z	S_{178}/Jy	α_{151}	$\theta/arcsec$
3C172	0.519	16.45	0.822	101.00
3C173.1	0.292	16.78	0.898	61.00
3C175	0.768	19.18	0.983	48.00
3C175.1	0.920	12.42	0.597	7.00
3C181	1.382	15.80	0.656	5.70
3C184	0.994	14.38	0.594	4.80
3C184.1	0.119	14.17	0.686	182.00
3C186	1.063	15.36	0.667	1.60
DA240	0.035	23.21	0.770	2164.00
3C190	1.197	16.35	0.786	6.70
3C191	1.956	14.17	0.907	4.90
3C192	0.059	22.99	0.810	196.00
3C196	0.871	74.33	0.590	10.00
3C200	0.458	12.31	0.829	26.00
4C14.27	0.392	11.22	1.150	38.00
3C204	1.112	11.44	1.118	36.60
3C205	1.534	13.73	0.736	18.00
3C207	0.684	14.82	0.803	14.00
3C208	1.11	18.31	0.766	11.00
3C212	1.049	16.45	0.785	9.00
3C215	0.411	12.42	0.928	59.00
3C216	0.67	22.01	0.630	30.00
3C217	0.897	12.31	0.769	12.00
3C219	0.174	44.90	0.798	189.00
3C220.1	0.62	17.22	0.946	30.00
3C220.3	0.685	17.11	0.682	7.40
3C223	0.136	16.02	0.807	306.00
3C225B	0.582	23.21	1.095	4.60
3C226	0.817	16.35	0.861	35.00
4C73.08	0.0581	15.58	0.850	947.00
3C228	0.552	23.76	0.713	47.20
3C234	0.184	34.22	0.885	110.00
3C236	0.0989	15.69	0.870	2440.00
3C239	1.781	14.38	0.857	11.20
4C74.16	0.568	12.75	0.870	40.00
3C241	1.617	12.64	0.481	0.91
3C244.1	0.428	22.12	0.802	53.00
3C245	1.029	15.69	0.670	9.10
3C247	0.748	11.55	0.565	13.00
3C249.1	0.311	11.66	0.872	44.10
3C252	1.103	11.99	1.085	60.00
3C254	0.734	21.69	0.752	13.10
3C263	0.646	16.56	0.754	44.20
3C263.1	0.824	19.83	0.692	6.80

IV

Name	z	S_{178}/Jy	α_{151}	$\theta/arcsec$
3C265	0.811	21.25	0.963	78.00
3C266	1.275	12.09	0.758	4.50
3C267	1.14	15.91	0.806	38.00
3C268.1	0.973	23.32	0.702	46.00
3C268.3	0.371	11.66	0.449	1.56
3C268.4	1.40	11.22	0.660	10.90
3C270.1	1.519	14.82	0.866	12.00
3C274.1	0.422	17.98	0.936	158.00
3C275.1	0.557	19.94	0.819	18.80
3C277.2	0.766	13.08	0.814	58.00
3C280	0.997	25.83	0.724	14.50
3C284	0.239	12.31	0.889	175.00
3C285	0.079	12.31	0.786	183.80
3C286	0.849	27.25	-0.401	3.80
3C287	1.055	17.76	0.217	0.09
3C289	0.967	13.08	0.630	10.00
3C292	0.713	11.00	0.800	133.00
3C293	0.045	13.84	0.614	216.00
3C294	1.786	11.22	1.022	15.00
3C295	0.461	91.01	0.285	5.49
3C299	0.367	12.86	0.557	12.00
3C300	0.27	19.51	0.837	100.00
3C303	0.141	12.20	0.719	47.00
3C309.1	0.904	24.74	0.388	2.90
3C318	1.574	13.40	0.518	0.80
3C319	0.192	16.67	0.852	105.00
3C321	0.096	14.71	0.825	307.80
3C322	1.681	11.00	0.800	33.00
3C324	1.206	17.22	0.680	10.00
3C325	1.135	17.00	0.671	16.00
3C326	0.088	22.23	0.880	1190.00
3C330	0.55	30.30	0.548	62.00
3C241	1.617	12.64	0.481	0.91
3C244.1	0.428	22.12	0.802	53.00
3C245	1.029	15.69	0.670	9.10
3C247	0.748	11.55	0.565	13.00
3C249.1	0.311	11.66	0.872	44.10
3C252	1.103	11.99	1.085	60.00
3C254	0.734	21.69	0.752	13.10
3C263	0.646	16.56	0.754	44.20
3C263.1	0.824	19.83	0.692	6.80
3C265	0.811	21.25	0.963	78.00
3C266	1.275	12.09	0.758	4.50
3C267	1.14	15.91	0.806	38.00

Name	z	S_{178}/Jy	α_{151}	$\theta/arcsec$
3C334	0.555	11.88	1.026	58.00
3C336	0.927	12.53	0.832	21.70
3C337	0.635	12.86	0.857	44.70
3C340	0.775	11.00	0.709	46.70
3C341	0.448	11.77	0.863	80.00
3C343	0.988	13.51	0.014	1.10
3C343.1	0.750	12.53	0.265	0.38
3C349	0.205	14.49	0.739	88.00
3C351	0.371	14.93	0.631	75.00
3C352	0.805	12.31	0.845	13.00
3C356	1.079	12.31	0.870	75.00
4C16.49	1.296	11.44	1.000	16.00
4C13.66	1.45	12.31	0.810	6.00
3C368	1.132	15.04	1.004	7.90
3C380	0.691	64.74	0.627	20.00
3C381	0.16	18.09	0.729	74.00
3C382	0.057	21.69	0.823	186.00
3C388	0.09	26.81	0.683	50.80
3C390.3	0.056	51.77	0.755	229.00
3C401	0.201	22.78	0.635	24.10
3C427.1	0.572	28.99	0.876	28.00
3C432	1.805	11.99	0.780	13.00
3C433	0.101	61.25	0.719	65.60
3C436	0.214	19.40	0.855	108.00
3C437	1.48	15.91	0.499	34.40
3C438	0.29	48.72	0.822	22.40
3C441	0.707	13.73	0.637	36.70
3C452	0.081	59.29	0.825	272.00
3C454	1.757	12.64	0.900	1.30
3C455	0.543	13.95	0.709	4.00
3C457	0.428	14.27	1.229	205.00
3C469.1	1.336	12.09	1.102	74.00
3C470	1.653	11.00	0.710	24.00

Table 1: Parameters of 3CRR sample used in our work. Column 1: 3CRR source name. Column 2: redshifts of the sources. Column 3: Flux density at $178Mhz$. Column 4: Spectral index between $178MHz$ and $151MHz$. Column 5: Angular size in arcseconds. The data is taken from Willot (2003)

Appendix 3: 6CE sample

name	redshift	S_{151MHz}/Jy	$\theta/arcsec$
0820+364	1.86	2.39	24
0822+341	0.41	3.06	18
0822+343	0.77	2.93	21
0823+375	0.21	3.35	81
0824+353	2.25	2.42	8
0825+345	1.47	2.10	7
0847+375	0.41	3.07	33
0857+390	0.23	2.71	24
0901+355	1.90	2.07	4
0902+341	3.40	2.14	5
0905+395	1.88	2.82	5
0908+373	0.11	2.33	39
0913+390	1.25	2.27	9
0919+380	1.65	2.72	10
0922+364	0.11	3.27	17
0930+385	2.40	2.21	5
0943+395	1.04	2.31	12
0955+384	1.41	3.45	22
1011+363	1.04	2.10	66
1016+363	1.89	2.28	31
1017+371	1.05	2.68	9
1018+372	0.81	2.52	83
1019+392	0.92	2.99	9
1025+390	0.36	2.97	1
1031+340	1.83	2.33	3
1042+391	1.77	2.68	11
1043+371	0.79	2.62	5
1045+340	1.83	2.00	22
1045+355	0.85	2.07	9
1045+351	1.60	3.03	0.1
1100+350	1.44	2.26	14
1108+395	0.59	2.10	16
1113+345	2.41	2.33	17
1123+340	1.25	3.40	0.2
1125+374	1.23	2.07	18
1129+371	1.06	2.36	19
1130+345	0.51	3.20	78
1134+365	2.13	2.07	17

name	redshift	S_{151MHz}/Jy	$\theta/arcsec$
1141+352	1.78	2.40	12
1143+370	1.96	2.06	0.1
1148+363	0.14	3.21	27
1148+384	1.30	3.83	10
1158+343	0.53	2.12	40
1159+365	1.40	2.20	2
1204+351	1.38	3.43	63
1205+391	0.24	3.83	24
1212+380	0.95	2.14	0.6
1213+350	0.86	2.39	0.1
1217+364	1.09	2.40	0.5
1220+372	0.49	2.52	36
1220+345	1.53	2.90	12
1232+394	3.22	3.27	51
1255+370	0.71	3.66	0.6
1256+364	1.13	2.88	18
1257+363	1.00	2.40	40
1301+381	0.47	3.46	28

Table 2: Parameters of 6CE sample used in our work. Column 1: 6CE source name. Column 2: redshifts of the sources. Column 3: Flux density at $151MHz$. Column 4: Angular size in arcseconds. The data is taken from Rawlings et al.(2001)

Appendix 4: 7CRS sample

Name	z	S_{151MHz}/Jy	$\theta/arcsec$
1731+6641	0.561	0.52	0.9
1732+6535	0.856	6.17	20
1733+6719	1.84	1.55	3
1736+6504	2.40	0.48	16
1736+6710	0.188	0.82	14.5
1740+6640	2.10	0.54	0.5
1741+6704	1.054	0.72	4
1742+6346	1.27	0.62	51
1743+6431	1.70	1.89	45
1743+6344	0.324	1.59	14
1743+6639	0.272	1.97	50
1745+6415	0.673	0.59	6
1745+6422	1.23	1.41	16
1745+6624	3.01	0.51	0.4
1747+6533	1.516	2.72	0.7
1748+6703	3.20	2.17	14
1748+6657	1.045	1.15	0.3
1748+6731	0.56	0.64	108
1751+6809	1.54	1.03	2
1751+6455	0.294	0.65	43
1753+6311	1.96	1.06	17
1753+6543	0.140	1.62	84
1754+6420	1.09	0.50	15
1755+6314	0.388	1.19	30
1755+6830	0.744	1.11	9
1756+6520	1.48	0.67	5
1758+6535	0.80	1.13	106
1758+6553	0.171	1.30	115
1758+6307	1.19	1.86	4
1758+6719	2.70	0.76	45
1801+6902	1.27	1.37	21
1802+6456	2.11	1.97	26
1804+6625	1.91	0.55	4
1804+6313	1.50	0.62	29
1805+6332	1.84	1.01	14
1807+6831	0.58	2.12	29
1807+6719	2.78	0.71	1.7
1807+6841	0.816	0.6	12

Name	z	S_{151MHz}/Jy	$\theta/arcsec$
1811+6321	0.273	0.95	52
1812+6814	0.816	0.6	23
1813+6846	1.03	1.51	52
1813+6439	2.04	0.50	38
1814+6702	4.05	2.26	14
1814+6529	0.96	1.22	126
1815+6805	0.230	1.96	50
1815+6815	0.794	1.37	200
1816+6710	0.92	2.36	27
1816+6605	0.92	1.29	2
1819+6550	0.724	1.17	9
1820+6657	2.98	0.83	0.4
1822+6601	0.37	0.97	52
1825+6602	2.38	0.84	3
1826+6510	0.646	1.39	34
1826+6704	0.287	0.60	19
1827+6709	0.48	1.10	17

Table 3: Parameters of 7CRS sample used in our work. Column 1: 7CRS source name. Column 2: redshifts of the sources taken from Lacy (1999). Column 3: Flux density at $151MHz$ taken from Lacy (1999). Column 4: Angular size in arcseconds taken from Lacy (1992).

Bibliography

Alexander P., 2000, MNRAS, 319, 8A

Alexander P., Leathy J.P., 1987, MNRAS, 225,1

Allen S.W., Dunn R.J.H., Fabian A.C., Taylor G.B., Reynolds C.S., 2006, MN-RAS, tmp, 964A

Baldwin J.E., 1982, in Heeschen D.S., Wade C. M., eds, Extragalactic radio sources. Reidel, p. 21

Barai P., Wiita P.J. 2006, MNRAS, tmp, 983

Barger A.J., Cowie L.L., Bautz M.W., Brandt W.N., Garmire G.P., Hornschemeier A.E., Ivison R.J., Owen F.N., 2001, AJ, 122, 2177

Begelman M.C., Cioffi D.F., 1989, ApJ, 345, L21

Best P.N., Rottgering H.J.A., Lehnert M.D., 1999, MNRAS, 310, 223

Best P.N., Rottgering H.J.A., Lehnert M.D., 2000, MNRAS, 315, 21

Best P.N., Peacock J.A., Brookes M.H., Dowsett R.E., Rottgering H.J.A., Dunlop J.S., Lehnert M.D., 2003, MNRAS, 346, 1021

Blandford R.D., Rees M.J., 1974, MNRAS, 169, 395

Blundell K.M., Rawlings S., 1999, Nature, 399, 330

Blundell K.M., Rawlings S., Willott C.J., 1999, AJ, 117, 677

Carroll S.M., Press W.H., Turner E.L., 1992, MNRAS, 30, 499

Dunlop J.S., Peacock J.A., 1990, MNRAS, 247, 19

Eales S.A. 1985, MNRAS, 217, 149

Falle S.A.E.G., 1991, MNRAS, 250, 581

Fanaroff B.L., Riley J.M., 1974, MNRAS, 167, 31P

Fasano G., Franceschini A., 1987, MNRAS, 225, 155

Gosset E., 1987, A&A, 188, 258

Grimes J.A., Rawlings S., Willott C.J., 2004, MNRAS, 349, 503

Hogg D.W., astro-ph/9905116

Jackson C.A., Wall J.V.,1999, MNRAS, 304, 160

Kaiser C.R., Alexander P. 1997, MNRAS, 286, 215(KA97)

Kaiser C.R., Dennett-Thorpe J., Alexander P. 1997, MNRAS, 292, 723(KDA97)

Kaiser C.R., Alexander P. 1999, MNRAS, 305, 707(KA99)

Lacy M., Rawlings S., Hill G.J., Bunker A.J., Ridgway S.E., Stern D., 1999, MN-RAS, 308, 1096

Leahy J.P., Williams A.G., 1984, MNRAS, 210, 929

Marconi A., Risaliti G., Gilli R., Hunt L.K., Maiolino R., Salvati M., 2004, MN-RAS, 351, 169

Manolakou K., Kirk J.G. 2002, A&A, 391, 127

McGilchrist M.M., Baldwin J.E., Riley J.M., Titterington D.J., Waldram E.M., Warner P.J., 1990, MNRAS, 246, 110

Miller C.J., Nichol R.C., Gomez P.L., Hopkins A.M., Bernardi M., 2003, ApJ, 597, 142

Neeser M.J., Eales S.A., Lawgreen J.D., Leahy J.P., Rawlings S., 1995, ApJ, 451, 76N

Owen F.N., Ledlow M.J. 1994, ASPC, 54, 319O

Peacock J.A., 1983, MNRAS, 202, 615

Peacock J.A., 1985, MNRAS, 217, 601

Rawlings S., Eales S.A., Lacy M., 2001, MNRAS, 322, 523

Scheuer P.A.G., 1974, MNRAS, 166, 513

Shklovskii L.S., 1963, Sov. Astr., 6, 465

Shu F.H.,1991, The physics of astrophysics. Vol.1: Radiation. University Science Books

Ueda Y., Akiyama M., Ohta K., Miyaji T., 2003, ApJ, 598, 886

Willott C.j., Rawlings S., Blundell K.M., Lacy M., Eales S.A., 1998, MNRAS, 300, 625

Willott C.j., Rawlings S., Blundell K.M., Lacy M., Eales S.A., 2000, MNRAS, 316, 449

Willott C.j., Rawlings S., Blundell K.M., Lacy M., Eales S.A., 2001, MNRAS, 322, 536

Willott C.j., Rawlings S., Blundell K.M., Lacy M., Hill G.J., Scott S.E. 2002, MNRAS, 335, 1120